Development of a single photon detector for fluorescent spectrometry

A Dissertation Presented

by

Dmytro Gudkov

to

The Graduate School

in Partial Fulfillment of the

Requirements

for the Degree of

Doctor of Philosophy

in

Electrical Engineering

Stony Brook University

December 2013

Stony Brook University

The Graduate School

Dmytro Gudkov

We, the dissertation committee for the above candidate for the

Doctor of Philosophy degree, hereby recommend

acceptance of this dissertation.

Vera Gorfinkel – Dissertation Advisor

Associate Professor, Department of Electrical and Computer Engineering

Dmitri Donetski

Assistant Professor, Department of Electrical and Computer Engineering

Leon Shterengas

Assistant Professor, Department of Electrical and Computer Engineering

Dmitriy Beznosko

Nazarbayev University

This dissertation is accepted by the Graduate School

Charles Taber
Dean of the Graduate School

Abstract of the Dissertation

Development of a single photon detector for fluorescent spectrometry.

by

Dmytro Gudkov

Doctor of Philosophy

in

Electrical Engineering

Stony Brook University

2013

I present a novel multichannel single photon detector based on PMT sensor (32-channel Hamamatsu H7260-20) with unique linearity range for applications in life sciences.

My extensive study of pulse characteristics of the PMT sensor showed that maximum linearity range obtained with 32-channel PMT could not exceed 10^8 counts/sec due to distortions of photon pulses at high input optical power.

Due to a novel, highly advanced analog/digital circuitry operating in GHz range, the developed 32-channel detector has a unique performance: it supports detection of up to 10^8 photons/sec per channel, data acquisition rate at up to 10^6 frames/sec, data transfer via Ethernet and data recording speed up to 32MB/sec.

Utilizing outstanding performance characteristics of the detector it was made possible to develop a unique single photon spectrometer. Having an extremely broad linearity range and high data acquisition speed, the spectrometer has been successfully used for the detection of fluorescent radiation from both single quantum dots (QD) and micro-beads with embedded quantum dots of different colors. Our experiments demonstrated the ability of the spectrometer to detect up to 10000 micro-particles per second. For the beads with embedded quantum dots of 6 different colors we were able to distinguish up to 10^5 different color combinations (QD fluorescence in spectral range between 490nm and 700nm).

Currently, in the field of the molecular biology there is a wide variety of techniques and assays based on color labeled micro- and nano-particles. The unique detection performance of our single photon sensor suggests its successful use in multiple applications such as life sciences, molecular diagnostics, personalized medicine and others.

TABLE OF CONTENTS

LIST OF FIGURES

LIST OF TABLES

LIST OF ABBREVIATIONS

Abbreviation or Symbol	**Term**
APD	Avalanche Photodiode
CE	Capillary Electrophoresis
DC	Dark Counts
OD	Optical Density
PCB	Printed Circuit Board
PCR	Polymerase Chain Reaction
PMT	Photomultiplier Tube
SiPM	Silicon Photomultiplier
SPAD	Single Photon Avalanche Diode

CHAPTER 1

TEORY OF QUANTUM PARTICLES DETECTION IN FLUORESCENCE SPECTROMETRY

1.1 Technology overview.

Over the years fluorescence spectrometry had become one of the primary methods of analysis in biochemistry and biophysics. Its high sensitivity and relative ease of use comparing to radioactive tracers method have brought it a widespread attention and appreciation in many life sciences applications.

Many different technologies have been developed to detect weak fluorescent signals while techniques relying on putting special fluorescent markers on microparticles carrying test substances have become more and more popular in the field of molecular diagnostics because of their simplicity, high sensitivity and specificity, and economic performance.

Recently a number of technologies have been developed for optical “bar coding” of micro objects (beads, cells, etc.) with nano particles. This includes the use of segmented nanorods [1], rare-earth doped glass [2], fluorescent silica colloids [3], photobleached patterns [4], enhanced Raman nanoparticles [5] and semiconductor quantum dots (QD) [6].

While each of the above technologies has its advantages and limitations, luminescent QDs exhibit nearly ideal properties for optical bar coding. Indeed, QDs’ fluorescence emission wavelengths can be tuned continuously by changing the QD size, and a single short-wavelength excitation source can be simultaneously used for exciting multiple colors. High-quality semiconductor-based QDs have relatively narrow and symmetrical emission spectra and are also stable against photobleaching [7]. In principle, at the present state of technology combinations of multiple QD colors and intensities can be used to encode billions of micro objects. However, practical solution for fast detection and decoding of billions of distinct color codes is an engineering challenge.

In this dissertation I will describe a novel instrument - single photon spectrometer – which allows an extremely fast, highly sensitive and accurate detection and recognition of QD-barcoded objects. We shall also present a method which enables an accurate separation of fluorescent signals emitted by individual components of the QD mixes. The linearity dynamic range of the detector's channels exceeds 10^7 photocounts per second and can be enhanced by a factor of 10 with the proposed signal processing algorithms.

1.2 Encoded multicolor particles detection.

Multiplex technologies which allow multiple discrete assays to be performed simultaneously within the same microvolume sample are promising tools in the field of molecular biology and medicine. Multiplex assays typically include screening chemical libraries for compounds of interest and screening for particular target molecules, such as antigens, antibodies, nucleotides and peptides, in test samples. The thousands of individual reactions that are required for these purposes are preferably carried out all at the same time.

One of the most important challenges in developing multiplex assays is the necessity to track each reaction. There are two main approached to do this. In the first approach, each reaction is physically separated — as it is done in 'high-density' DNA arrays or microchips. In the second strategy, the reactions are carried out on individual microcarriers — each carrier having a particular molecule bound to its surface. In the first approach, the identification of the molecule that is analyzed is determined by the exact location on the microarray. The second approach requires each of the microcarriers to be labeled to allow the identification of molecules bound to their surface. This method allows uniquely encoded microcarriers to be mixed and subjected to an assay simultaneously.

Currently, there are four major groups of methods used for encoding microcarriers: optical, electronic, graphical and physical encoding. The most important characteristics for any encoding method include the number of microcarriers that can be uniquely encoded, size of the microcarrier, and the ability to rapidly and automatically encode and decode the microcarriers. These parameters, in conjunction with the cost of the techniques, determine which encoding strategy will be broadly used for commercial applications.

The electronic encoding methods are based on the use of radio frequency memory tags. An encoded microcarrier comprises a microelectronic chip with an embedded non-volatile unique digital code. When the microcarrier passes a detection zone, the microchip gets activated (electronically or optically) and transmits its ID code as an RF signal. Typical 40-bit code can provide ~10^{12} unique ID combinations. Major disadvantage of the electronic encoding is relatively large size of microcarriers ranging from millimeters to hundred microns.

The graphical encoding [1] is based on storing information by spatial modulation of a material of the microcarrier or its properties. Among many graphical encoding techniques, the most promising are graphical-encoded metal particles. The metal cylindrical rods consist of adjacent (submicron) stripes of alternating metals. The minimal useful stripe length is determined by the optical detection resolution, and is estimated to be ~500 nm. The diameter of the rods is between 15 nm and 12 mm, and the overall length of the particles will be between 1 and 50 mm. The number of uniquely encoded rods is virtually unlimited, since many parameters can be varied. The detection can be automated by sending the particles through a cytometer-like system. However, all particles produced in the same process will have identical codes because they were created by the same electrochemical reduction steps (~30min per step). So, to create one million different codes, the process must be repeated one million times.

In optical encoding method, microcarriers can be identified by their absorption or emission spectra as well as by the fluorescence decay time.

In one of the most developed color encoding strategy, the optical codes are created by incorporating distinct proportions of different fluorescent dyes. The ideal dyes should have both coinciding excitation spectra and clearly separated emission bands. Nevertheless, even with the relatively limited degree of multiplexing, the technique has proved to be of great use in many applications, including genotyping, measuring cytokine cadmium and thyroid levels, cysticfibrosis screening, genetic human lymphocyte antigen (HLA) typing, kinase testing and allergy testing.

Many of the problems related to organic dyes are largely overcome by using fluorescent semiconductor quantum dots (QD) [7]. Conventional dye molecules have a narrow excitation spectrum, which makes simultaneous excitation of different dyes difficult, and their broad emission spectrum with a long tail at red wavelengths introduces spectral crosstalk between different detection channels. This makes quantification of the relative amounts of different dyes difficult. By contrast, semiconductor QDs have a continuous excitation spectrum, and an emission spectrum that can be continuously tuned by changing the particle size. Their emission spectrum is very narrow (typically 20–30 nm). Therefore, many sizes of QDs can be excited simultaneously with only one wavelength of light, resulting in many emission colors with minimal spectral overlap. Moreover, the quantum dots are more photochemically stable in comparison to conventional fluorophores [7].

However, until recently, brightness and uniformity of encoding signals did not allow identification of microcarriers at high speeds and high accuracies. The breakthrough in this field was made with an advent of a new generation of mesoporous polystyrene beads encoded with surfactant-coated (hydrophobic) quantum dots Prepared by a multiple-stage polymerization process, this class of porous beads is highly uniform in size and contains an extensive network of nanometer-sized pores. These “mesoscopic” pores allow rapid uptake and immobilization of quantum dots through strong hydrophobic interactions between the pore walls and the QD capping ligands (tri-n-octylphosphine oxide, TOPO) [8]. These beads may contain up to several million quantum dots and produce very bright fluorescence (2x104 photons per mW per second per 1 quantum dot).

We would like to emphasize that although at the present state of QD technology billions of distinct color codes can be realized (*9 QD types at 10 intensity gradations would yield* 10^9 *color codes*), commercially available sets of beads now contain maximum up to hundred distinct codes. Several reasons limit the number of codes including spectral overlapping, fluorescence-intensity variations and signal-to-noise requirements.

In conclusion, in terms of the number of codes, the graphical and electronic encoding strategies are the most promising. Optical encoding strategies, on the other hand, have the advantage of being easier to fabricate, encode and decode microcarriers, since only the overall optical properties of the particles need to be detected.

1.3 Processing of fluorescence spectra.

The main task of the signal processing is the determination of concentrations of individual fluorescent dyes in dye mixtures composed of *n* dyes having distinct and known fluorescent spectra. The concentrations of individual dyes in the mixture can be found by a decomposition of the fluorescence measured in *N* independent channels of the spectrometer, provided the spectrometer produces linear response to the detected fluorescence.

Let us assume that the number of the analyzed fluorescent dyes $n \leq N$ (e.g. n=4 for DNA sequencing). Let us introduce the system matrix $\mathbf{H}_{(N \times n)} = (\mathbf{h}_1, \mathbf{h}_2, ..., \mathbf{h}_n)$ where $\mathbf{h}_i = (h_{1i} \; \dots \; h_{Ni})^T$, $(1 \leq i \leq n)$ are N-component vectors representing spectra of the fluorescent dyes in the analyzed dye mixture. In order to obtain a system matrix **H** one has to perform the system calibration and measure in advance spectral responses of individual fluorescent dyes $\mathbf{h_i}$. If $\mathbf{r} = (r_1 \; \dots \; r_N)^T$ is the measured fluorescent spectrum of the dye mixture, and $\mathbf{s} = (s_1, s_2, ..., s_n)^T$ is a vector of component weights representing concentrations of individual fluorescent dyes, than in the presence of noise $\boldsymbol{\omega} = \left(\omega_1 \; \dots \; \omega_N\right)^T$ the measured spectrum

$$\mathbf{r} = \mathbf{Hs} + \boldsymbol{\omega} \,. \quad (1)$$

The optimal solution $\mathbf{s}$ of the Eq. (1) depends on the assumption regarding the distribution properties of the noise components ω_i. Simplified assumption about ω_i being independent identically distributed normal random values yields well known and computationally efficient minimum variance unbiased solution for estimate $\hat{\mathbf{s}}$:

$$\hat{\mathbf{s}} = \left(\mathbf{H}^T\mathbf{H}\right)^{-1}\mathbf{H}^T\mathbf{r}. \quad (2)$$

In photon counting, individual rate observations r_i have Poisson distribution with equal mean and variance. For higher photocount rates (over 50 counts per observation period), the observed rates are well approximated by superposition of ‘true’ mean rate $\overline{r}_i$ and Gaussian noise ω_i with variance depending on the mean rate:

$$r_i = \overline{r}_i + \omega_i, \quad \omega_i \sim N\left(0, f\left(\overline{r}_i\right)\right).$$

Thus, more precise solution can be obtained by assuming the components ω_i independent non-identically distributed normal random variables. The general solution for Eq.(1):

$$\hat{\mathbf{s}}^* = \left(\mathbf{H}^T\mathbf{C}^{-1}\mathbf{H}\right)^{-1}\mathbf{H}^T\mathbf{C}^{-1}\mathbf{r}, \quad (3)$$

where $\mathbf{C}$ is the covariance matrix of components ω_i. Due to independence of ω_i the matrix $\mathbf{C}$ is diagonal:

$$\mathbf{C} = \begin{pmatrix} \sigma_1^2 & & & 0 \\ & \sigma_2^2 & & \\ & & \ddots & \\ 0 & & & \sigma_N^2 \end{pmatrix}, \quad (4)$$

where σ_i^2 is the variance of ω_i. In practice, mean rate $\overline{r}_i$ is unknown and observed rate r_i is used for the computation of the variance:

$$\overline{r}_i \approx r_i.$$

Variances σ_i^2 are estimated for each measurement. The function that relates σ_i^2 and r_i is specific for each preprocessing method used to obtain r_i. For example, if r_i are obtained directly by counting of photons during a sampling period, then $\sigma_i^2 = r_i$. If background b_i is subtracted from the result of the counting observation, then $\sigma_i^2 = r_i + b_i$. If r_i is obtained by averaging counting observation over k sampling periods, then $\sigma_i^2 = r_i / k$. The estimator (3) is more accurate, but requires more computational resources than the estimator (2).

The approach described above allows construction of the procedure, which performs background subtraction at the stage of cross-talk removal. This is achieved by creating additional spectrum (column in matrix $\mathbf{H}$) that represents the background. The estimators (2) and (3) with new matrix $\mathbf{H}$ will separate the background from the other spectral components.

Detailed description of the technique and application results can be found in [10].

1.4. Single photon detectors for laser-induced fluorescence.

Fluorescence represents a very low light, of about femtowatts intensity. But, at the same time laser excitation power lies in range of miliwatt. A huge dynamic range detector would be required to cover all possible fluorescence levels.

The power of one picowatt is equal to a photon flux of ~10^7 photons per second. So if the response time of the photon detector to each incoming photon is much less than 10^{-7} second, the detector will see the photon flux as discrete particles. Responding to each single photon, the detector gives an output pulse with amplitude that depends on the internal gain of the detector. Main characteristic of a photon detector is its signal to noise ratio as depending on it a photon event is created. As we can’t affect signal intensity, getting the least noisy detection system is an ultimate goal. Absolute minimum noise of photon detection systems is defined by the Poisson fluctuation due to the stochastic process of avalanche multiplication. Single photon detectors are approaching this lower limit.

There’re a number of key criteria a single photon counting detector should satisfy:

- Lowest possible dark count noise.
- Fast response time, to be able to recover after processing one photon event for the next one.

- Large linear dynamic range, to be able to register events of different light magnitude while having a predictable response.
- Spectral range covering large part of 400-1000nm scale, which is typical wavelengths of signals in microbiology applications.
- High sensitivity to the photon events, typically governed by quantum efficiency of the detector.
- Large active area, to overcome coupling losses.
- Multiple parallel channels to be able to register different events happening simultaneously or to provide high spectral resolution in case of multichannel spectrometer.

The subject of this dissertation is to describe PMT-based single photon spectrometer having exceptional performance characteristics majorly in counting rate and dynamic range.

1.5 Brief comparison of single photon detectors.

Widely available single photon detectors include PMTs, SPADs and SiPM. While SiPMs are gaining popularity in recent years as a very cheap and potentially efficient photon detectors their relative small detection area and complications with high dark noise still allow PMT to stay as the most widely used and versatile detector. Judging from the Table 1.1 drawbacks of PMTs in comparison to other types of detectors are high supply voltage and low photodetection efficiency, though large photosensitive area, commercial availability of multichannel PMTs and novel approach leading to ~100Mil max count rate presented in this dissertation allow them to be a detector of choice for many fluorescence detection approaches.

Performance parameter	**PMT**	**SPAD**	**SiPM**
Spectral response range	200~900	200~1000 nm	300 ~1000 nm
Photosensitive diameter	large	0.1~0.5mm	0.1~3mm
Gain	10^6	10^6	10^6
Power supply	~KV	~200V	~50V
Price	~$200	~$1000	~$10
Dynamic range	~10M	~10M	10~100M
Temperature coefficient	_	0.7V/ºC	0.05V/ºC
Processing technology	Vacuum tube	Dedicated	Standard CMOS
PDE	5~20%	20~70%	20~70%
Gain varies with magnetic field	yes	no	no

Table 1.1 Comparisons: PMT, SPAD, and SiPM

1.6 Formulation of system requirements.

Our beads coloring strategy requires the ability to distinguish millions of color combinations. Problem with detecting color combination from micro-beads is that the beads are moving very fast (1-2m/s) and they emit very low amount of light.

Our solution is to develop a single photon detection with broad linearity range, fast frame rate and high data recording rate.

For a beads detection system our ultimate goal is to deliver up to 10^4 objects/s which have to be recognized with 1%-10% accuracy. In order to be able to do that we need to collect about 10000 photons per dye. Since in our spectrometer a dye spectra occupy ~ 5-6 photocathodes of PMT, our total requirements for the system goes up to having ~10^8 counts per second total. This requirement is the basis on which all the further discussed development of single photon spectrometer is based.

CHAPTER 2

DEVELOPMENT OF SINGLE CHANNEL PHOTON COUNTER

2.1 Description.

Single channel counter was the first step on the way to 32-channel high speed counter we had in mind from the start. The idea behind single channel counter was to develop the counter being able to reliably count PMT pulses from tens (right above noise floor of the PMT) up to 100 million counts per second. Upper bound was limited by ~1ns PMT pulse width and best possible switch rates of the necessary circuitry. As PMT pulses as well as photon flux incident on PMT window obeyed Poisson distribution as the number of pulses increase more and more pulses would overlap and merge with each other reducing the amount of registered photon events. Simple analysis would give us ~60% probability of having 2 or more pulses in 2ns interval at 1Ghz photon rate thus making photon counting not applicable there. At 100MHz on the other hand this probability gets reduced to only 1.7% for *initial* photon flux. This way in the ideal case when amplifying and discriminating circuits would add to noise and pulse spread to this figure, reliable counting at 100MHz would be easily possible.

According to the numbers above the faster and less noisy components we would use the closer we would be to 100 million count goal. Having that in mind we ended up with Infineon technologies 20-db BGA427 amplifiers and Analog Devices ADCMP553 LVPECL comparators for pre-amplification and discrimination circuits respectively.

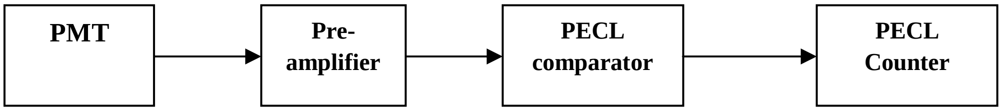

Figure 2.1 Single channel block diagram.

We can divide our processing circuit into 3 major functional blocks:

- Pre-amplifier circuit;
- Comparator;
- Pulse counter.

Over the course of development of single channel counter and, especially, the much more advanced 32-channel counter the exact types of components used in each of those blocks did changed fitting to the requirements of the device, but the very functional structure remained the same. Pre-amplifier circuit’s purpose is to increase the magnitude of comparably weak PMT pulses to the triggering levels of the subsequent comparator. The exact amplification provided by this circuit has to be as low as possible to keep the pulses shape close to the original one and, at the same time, to be high enough to suit the input requirements of the subsequent comparator.

Comparator is used as a selective device to register pulses above a certain height and to cut off most of the PMT noise. This goal could be achieved by changing its threshold to the desired value.

Pulse counter has to be able to register and count all the pulses coming from the comparator and output the counted numbers into PC.

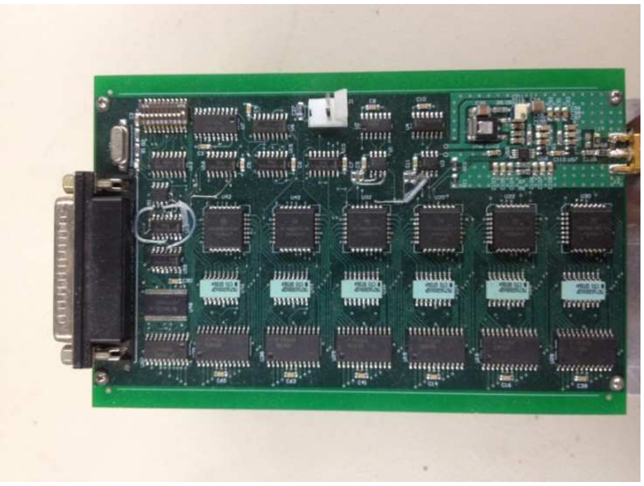

Figure 2.2 Top view on the counter board.

In the following chapters we will go into much more detailed description of each functional blocks of the single channel counter device.

2.2 Materials and methods.

2.2.1 Amplifier.

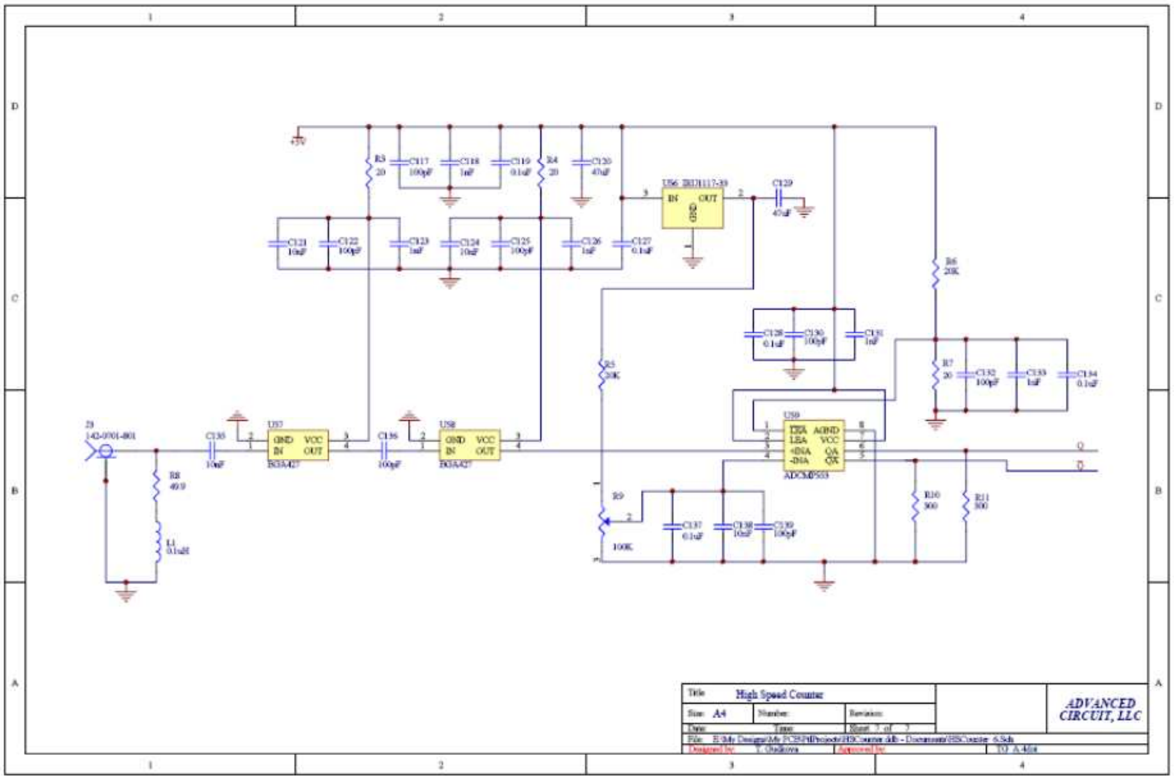

Figure 2.3 Amplification circuit scheme.

Magnitude of pulses produced by any PMT is governed by its internal gain, but even for the highest gain PMTs available on the market it lies within ~2-3x10^6 which corresponds to 10-50mV voltage pulses on 50ohm load. Pulses of that magnitude couldn't be feed directly into the digital circuits, thus they had to be pre-amplified to the necessary levels for the comparator to reliably trigger.

Since PMT produces current pulses as a result of multiple multiplication stages at the dynodes with some coefficient at each dynode and those coefficients can vary depending on many factors, pulses corresponding to different photons can have different magnitude. This fact along with finite tolerance of comparator threshold leads to the necessity of pre-amplification of the pulses into single volts range. On the other hand if the amplification ratio is too high, the largest pulses will get into saturation region of the amplifiers or will get out of higher bound of comparator input range – in both cases that will lead to broadening of the pulses and, thus, decreasing the maximum count rates which directly contradicts our goal.

That's why we tried different amplification schemes in order to find the optimal one. We started with 2-amplifiers circuit having 2 identical BGA 427 amplifiers (U57 and U58) in cascade, resulting in ~40db total amplification (Figure 2.3). Since each of the amplifier inverted the polarity of the pulse, the amplified pulses stayed negative. The amplified signal went to the ADCMP553 LVPECL comparator (U59). The reference voltage can be adjusted using potentiometer R9 from 0 to 3.3 volts. When the negative amplified signal pulse goes to the comparator, it generates PECL-level output pulse, which goes to the counters.

The further experiments have shown that 2 stage scheme was redundant and, moreover, led to spreading of output pulses width due to the 2nd stage amplifier was reaching its saturation region too often. That was an unfavorable result for us since we strived to introduce as little distortion of the PMT pulse as possible.

Next we went through the idea of putting an adjustable attenuator to the amplifier input (which ended up as too complicated and unnecessary) and finally after a sequence of test we gave up of the 2-stage scheme in favor of single amplifier one.

Accordingly for 1-stage amplifier we got rid of U57 amplifier and C35 capacitor. The resulting scheme provided 20dB amplification and changed polarity of the pulse only once. After the amplifier the positive pulse going to the comparator, whose reference voltage needs to be set from 1.2V (middle point of the amplifier) up to the amplified pulse height. According to our tests the threshold voltage had to be chosen as close to the pulse bottom as possible at the same time having it above the noise level. Values around 1350mV were found satisfying.

Less amplification in this implementation could potentially lead to losing some very small pulses in the noise floor, but their numbers were found to be negligible.

2.2.2 Comparator.

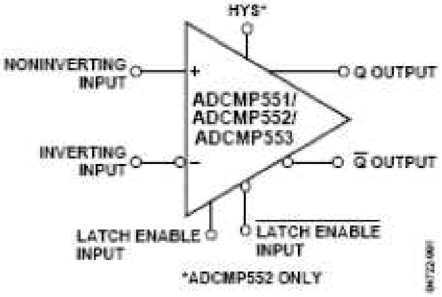

Figure 2.4 Comparator pin-out.

The choice of the comparator was one of the most important things to affect the whole performance of the device.

There have been 2 major requirements:

- highest possible switching rate;

- high noise protection.

Both requirements obviously served only one purpose - to alter the pulses characteristics as low as possible. That was the reason of choosing LVPECL logic. It provided us with exceptionally low rise and fall times (~500ps both) and very good RF noise reduction, due to differential outputs mode. Any transmission line carrying GHz signal for even a couple centimeters length encounter a lot of induced noise over the air, that’s why PCB layout and choice of transmission ways had to be done very carefully.

Choice of low voltage PECL logic was quite justified by trying to overcome an intrinsic drawback of PECL-family to have high power consumption.

2.2.3 Counter.

High Speed counter contains:

- Two identical counting circuit, each containing a **Three-byte PECL counter,** 3 **PECL to TTL 3-state buffer** and 3 **AND gates**.

- Synchronization circuit, containing a fixed value unit **Sync-byte, Sync-blocks two-byte counter,** 3 **3-state buffers** and 3 **AND gates.**

- Control circuit, containing a **Crystal oscillator, 14-stage binary ripple counter, Switches, Bytes Counter, Blocks counter**, 2 **AND gates**, 1 **NOT gate**, flip-flop **FF,** and 4 **TTL to PECL converter.**

- LPT output control circuit, containing **Time Delay unit, OR gates** and flip-flop **FF.**

High Speed Amplifier pulses simultaneously get to the inputs of **3-byte PECL counter #1** and **#2.** One of these counters is always in counting mode, while the other one is on hold and its accumulated data is being transferred byte after byte to the LPT port through the **PECL to TTL 3-state buffer,** corresponding to the byte number. **Three-byte PECL counter #1** and **#2** states are determined by the *control circuit* signals converted by the corresponding **TTL to PECL converters**.

TTL to PECL converter #2 output signal sets and holds the **Three-byte PECL counter #1** into the hold mode, and the **Three-byte PECL counter #2** - into the counting mode.

TTL to PECL converter #3 output signal sets and holds the **Three-byte PECL counter #2** into the hold mode and a **Three-byte PECL counter #1** - into the counting mode.

Converter #1 and #3 output signals reset the corresponding **Three-byte PECL counter** after its data has been transferred to the LPT port.

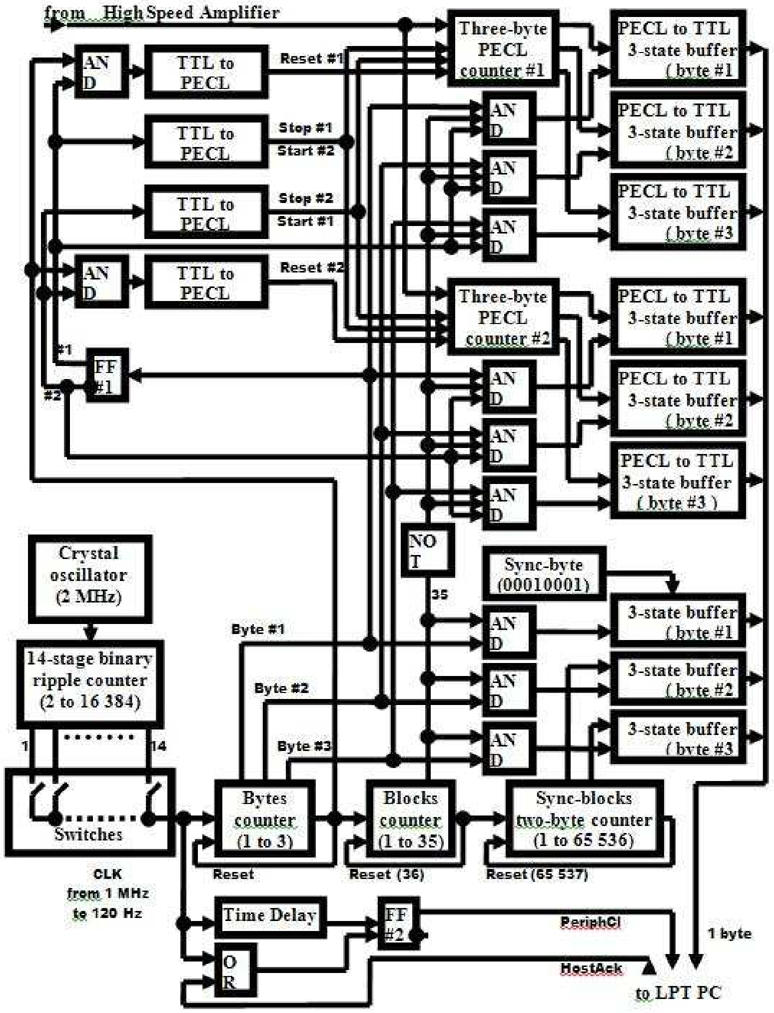

Figure 2.5 Counter block diagram.

After each 102 transmitted bytes there go the 3 synchro-bytes from the *synchronization circuit*. 1st byte has the fixed value of 00010001 and 2nd and 3rd bytes are the current state of the **Sync-blocks two-byte counter**. The synchro-bytes go the system output through the corresponding **3-state buffers.**

Crystal oscillator generates the 2 MHz clock pulses which go to the **14-stage binary ripple counter**. The counter has 14 output pins. Each pin outputs the clock pulses with the initial frequency divided by a coefficient from 2 to 16386. **Switches** are used to choose the pin and therefore the clock frequency for the whole circuit. **Switches** can set the transmission speed of the data to the LPT port from 122 to 1 000000 bytes per second.

The clock pulses get the **Bytes Counter**. After receiving each clock pulse the **Bytes Counter** sequentially generates the signal on its 3 outputs. Each signal allows the transmission of the corresponding data byte. Each of these signals goes to the both *counting circuits* and, via the corresponding AND gate – to the *synchronization circuit*.

The high on the 4th output resets the counter. It also goes to the **Blocks counter**, which counts the number of the transmitted 3-byte words. When the transmission of the 102th data byte ends (34-th 3-byte word) **Blocks counter** generates the signal for the 35th word. This signal allows #3 **AND gates** to transmit the signals for putting the synchronization circuit's data to the LPT output. At the same time this signal (for the 35th 3-byte word) blocks the output of the *counting circuits*.

Blocks counter output signal, corresponding to the 36th 3-byte word, resets the counter and clocks the **Sync-blocks two-byte counter,** which counts the number of 105 byte sequences and resets at a value of 65536.

Flip-flop **FF#1** triggers by every 1st byte pulse of the **Bytes Counter**. Its signals alternately put **Three-byte PECL counter #1 and #2** into count or hold modes, enable/disable the output of the counters and allows/block the transmission of the reset pulse to the counters via **AND #1-4** and **AND #1-4 gates.**

2.2.4 Software.

In order to be able to store and present the accumulated data in PC we developed a software package strictly dedicated to this purpose. It consists of recording software, real-time visualization package and offline visualization package.

For single channel counter we use LPT port to transfer the data into PC. Despite being a legacy port LPT allowed us to have the integration window as low as 1ms, which provided decent time resolution for optical counts.

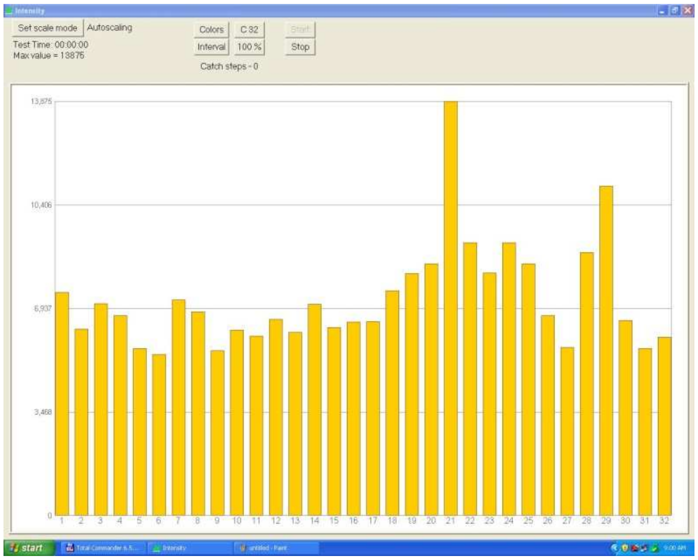

Set scale mode Autoscaling

Test Time: 00:00:00

Max value = 13876

Catch steps - 0

Figure 2.6 Intensity software window.

On the Figure 2.6 there's a screenshot of our 'Intensity' software. It was designed to provide a view of all the PMT channel at the same time. It is very useful to get picture of the current light conditions of the PMT and is extensively used for fine-tuning comparators' thresholds for all the channels.

Start time: 09:01:08
Test Time: 00:00:32

Figure 2.7 Monitor software main window.

The Figure 2.7 shows us ‘Monitor’ software window which serves the purpose of recording data from LPT and forming the output data file. It is also suited to provide real-time single channel monitoring, as it can be seen on the screenshot.

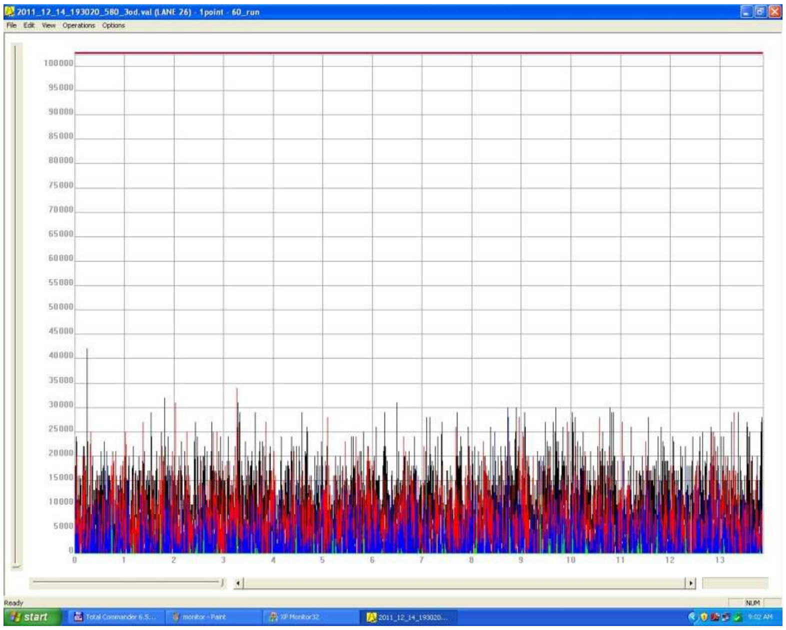

Figure 2.8 Base software main window.

And finally on Figure 2.8 we can see ‘Base’ software window which is used for offline analysis and processing of the recorded data files.

2.2.5 Optical system.

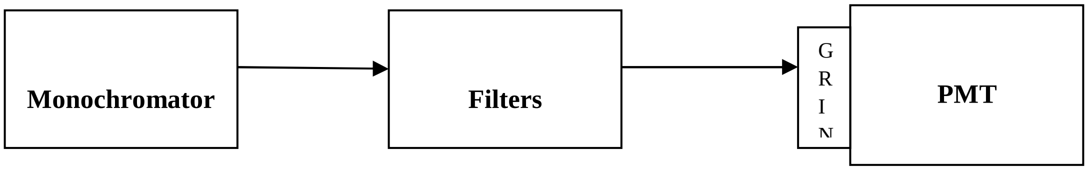

Figure 2.9 Optical system setup.

For our experiments we designed an optical system with 2 major capabilities:

- Light intensity is uniform and easily adjustable in the range from full darkness up to higher count limits of the system.
- Light spot hitting the PMT has to be as focused and confined as possible to be able to illuminate only 1 channel of the PMT.

First property was achieved by using The Optometrics Group MLM-2 monochromator which has an adjustable wavelength of the emitted light from 400nm up to 800nm. With this type of monochromator light can be easily attenuated by means of a set of neutral filters. In our case -5OD filter was almost equivalent to darkness conditions on the PMT. So using -4, -3, -2, -1 and -0.3 OD and 0 OD for no filters settings we managed to take most of our linearity curves.

Second property implementation involved a 200mkm fiber connecting SMA connector on the monochromator and a custom-made PMT header attached to the PMT front part.

Figure 2.10 PMT header before attaching to the PMT front.

The header was designed to be able to slide along the PMT front, thus directing the light on any PMT channel.

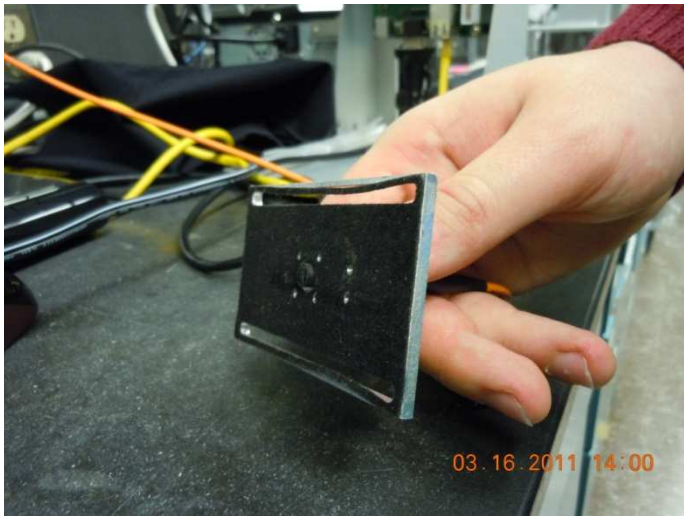

Figure 2.11 PMT header back side.

A GRIN lense was incorporated into the header to be able to focus the light onto the channel even more, thus reducing optical crosstalk by a noticeable margin.

CHAPTER 3

RESULTS DISCUSSION

3.1 PMT pulses.

Since PMT pulses width is ~1ns we had to use a high bandwidth oscilloscope to be able to capture the pulses shape. Tektronix TDS7404 4GHz oscilloscope was quite sufficient for this cause. Many of the pictures below were taken in accumulating mode of the oscilloscope which allowed us to view many pulses at once, thus displaying pulses height variations. Blue graph in the left part of the figures represents a pulses height distribution in the sample.

The following pulses have been obtained from 9th channel of the PMT for different light intensity levels. In the weak light conditions (4OD attenuation in our setup, Figure 3.1) we observed pulse height variations from ~5mV up to 70mV for single pulses. Though, according to the histogram average pulse height was at about 20mV with FWHM width of ~1ns, as it was expected for this type of PMTs.

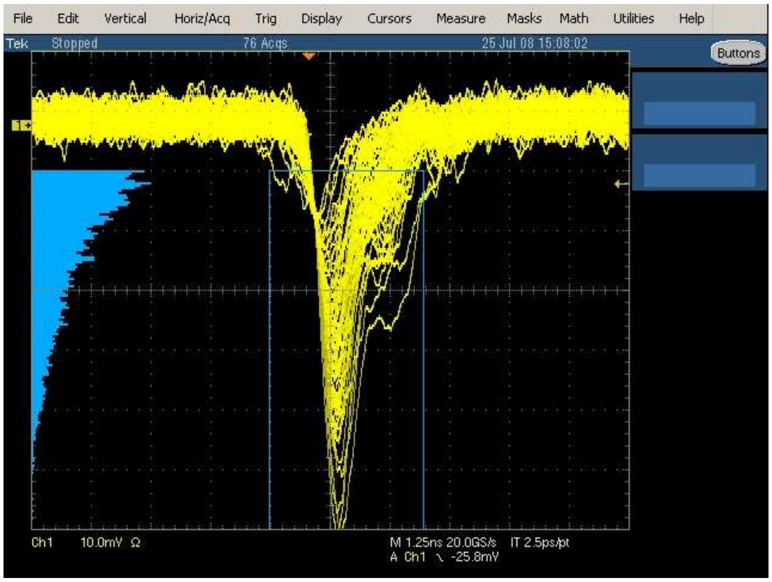

Figure 3.1 PMT pulses in weak light.

Next figure (Figure 3.2) displays pulses behavior in the oversaturation condition. Almost all the pulses are merged with the noise floor, and despite their amounts are very high our discriminator scheme is unable to register the most of them. If comparator threshold is high there're no pulses registered, if it's low real PMT pulses get mixed up with noise and counts are very high, giving us the noise picture.

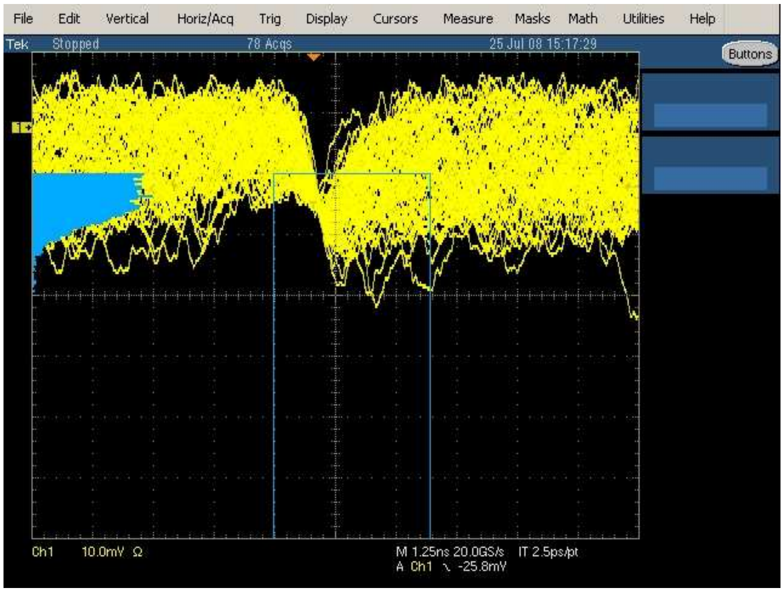

Figure 3.2 PMT pulses in very high light.

The Figure 3.3 shows changes in number of pulses and pulses heights occurring when a graduate increase in light intensity is performed. In can be easily seen that pulses stay 'valid' up to 1OD measurements (7th screenshot from top left on Figure 2.3), then an interesting behavior is observed. As the light increases further not only the number of pulses goes up, but their amplitude goes down as well. We explain it by PMT going out of its working conditions, thus producing many additional pulses per each real one. Though number of counts registered by the counter goes down, as most part of the pulses appears below its threshold (set up for working condition) and its ability to tell one pulse of another also gets reduced, since the pulses overlap each other.

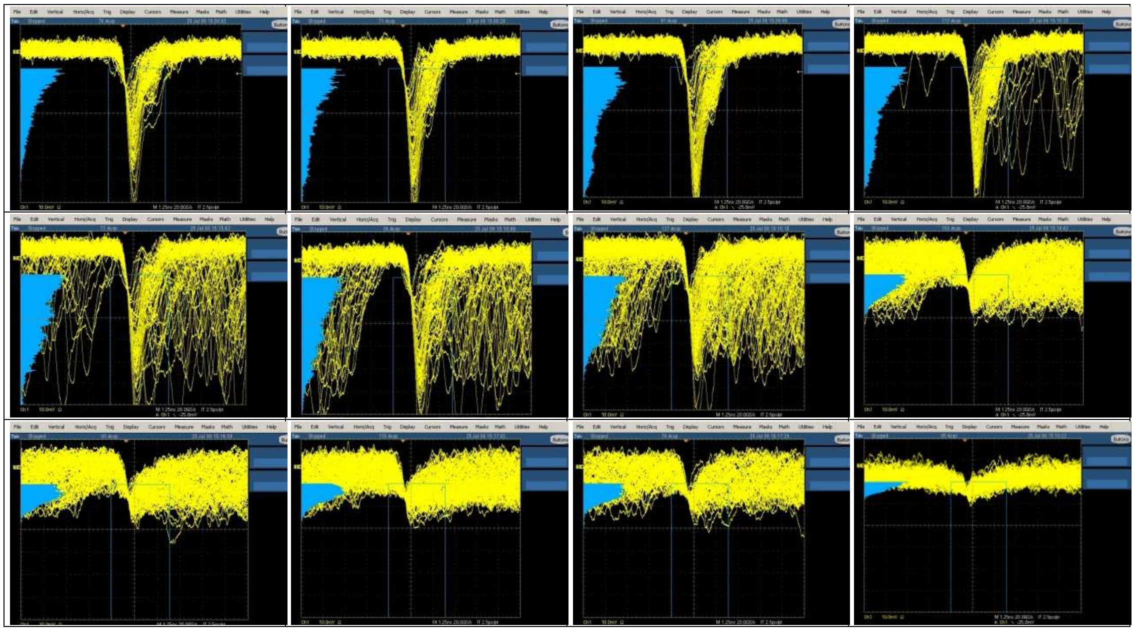

Figure 3.3 PMT pulses in the range from darkness to very high light.

Judging by the pulses shapes it’s reasonable to conclude that up to 1OD PMT has to be close to the linear mode. At 1OD the pulses are still close to the valid ones, by there has to be some deviations from linear characteristics and at higher light PMT behavior has to be highly non-linear. And it appears to be just the case in our linearity discussions in a chapter below.

3.2 PMT vs. Comparator pulses.

Since the performance of the whole system heavily relies on comparator switching capabilities it’s important to compare pulses going out of the comparator to the initial PMT pulses. This way we can tell how wider the pulses become after the comparator and thus what are the pulses our counters have to deal with.

We had 1-stage amplifier scheme and 2-stage amplifier scheme to test and compare.

3.2.1 One-stage amplifier.

On Figure 3.4 we can see pulses taken at the comparator output (cyan) versus pulses on the comparator input (yellow) for different light intensities and thus number of pulses. It appears that comparator pulses are at ~2ns width, compared with amplifier pulses of 1ns. This pulses widening was expected from comparator characteristics and is very good for pulses counting purposes. For any pulse height comparator response is unchanged.

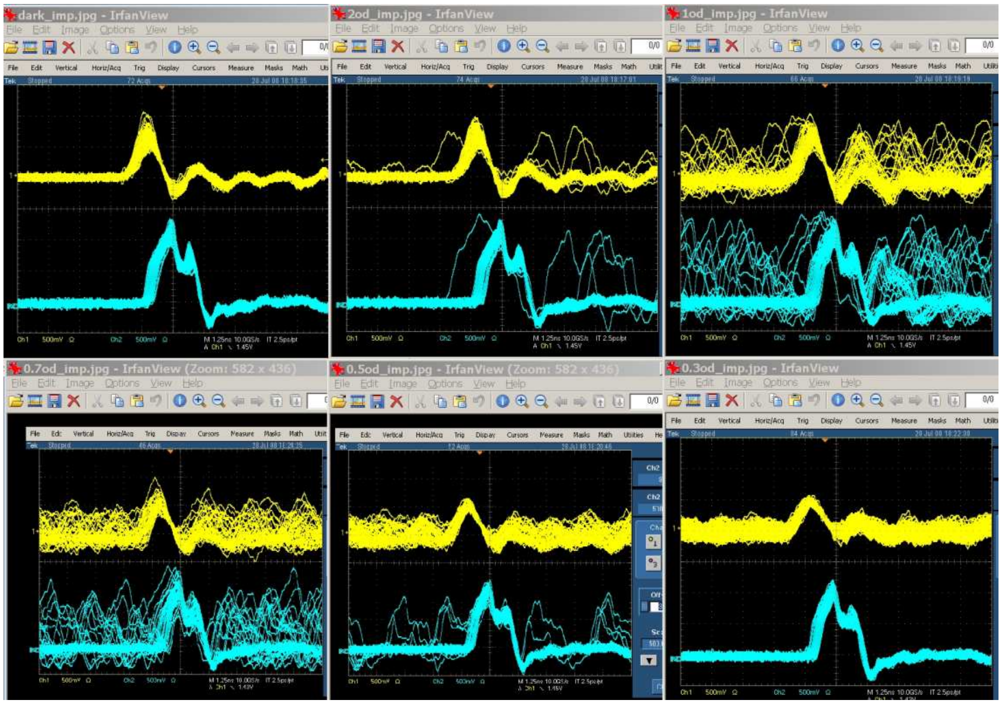

Figure 3.4 One-stage amplifier vs. comparator pulses.

3.2.2 Two-stage amplifier.

For our 2-stage amplifier, using the same optical part, we obtained the following pictures, clearly showing the spread of the pulses after comparator or, which is equivalent to the pulses width after 2nd amplifier added to <1ns increase by the very comparator.

At Figure 3.5 top 2 graphs PMT pulses are small and comparator output is close to 1-stage amplifier case above, but bottom 2 graphs of Figure 3.5 shows what happens if the pulses are large. Comparator pulses became much wider (about 5ns) than expected and reasonable to use.

We investigated this rather unexpected spread and found out that the cause of it is the fact the amplification is too large. The pulses after first amplifier put the second amplifier’s transistors into saturation region causing the spread. This performance was found unacceptable and we gave up with 2-stage amplifier scheme altogether.

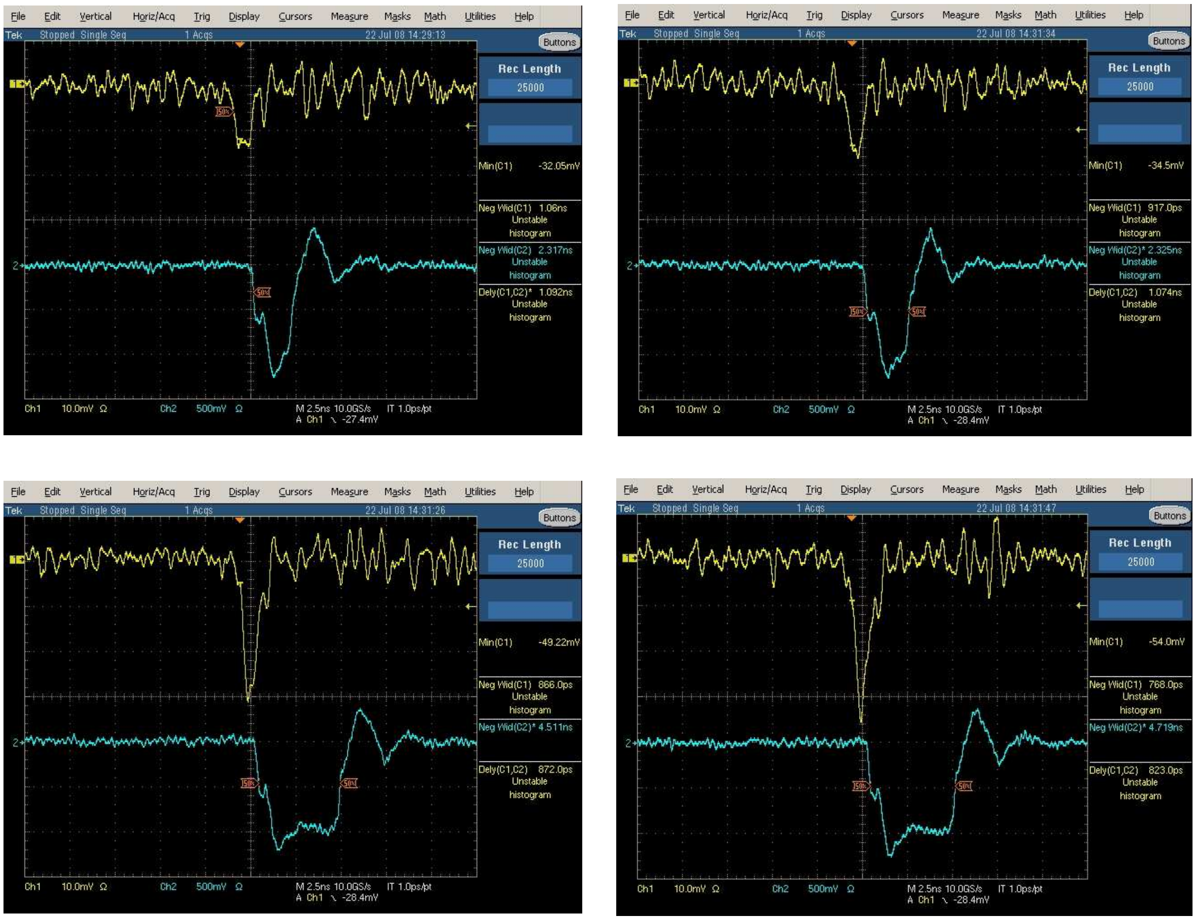

Figure 3.5 Two-stage amplifier PMT vs. comparator pulses.

3.3 PMT counts linearity.

Our goal of achieving 100 million counts per second is two-fold. First we need to demonstrate the very ability to get to 10^8counts and second, which is equally important, to show that that high counts lie within linear range of the device. That’s why linearity measurements are the key performance characteristics of the counter.

We assembled the setup on figure 3.6 for linearity measurements.

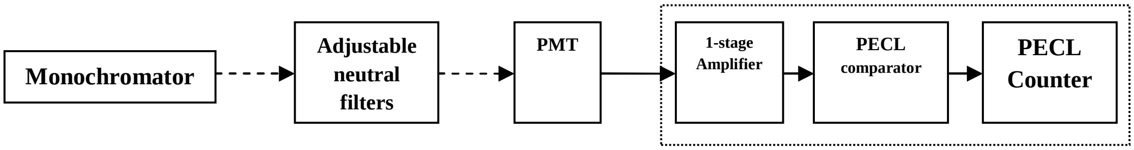

Figure 3.6 Linearity measurements setup.

Then we fixed the wavelength in the area of high PMT response and went through our set of filters at -4, -3, -2, -1, -0.3 and 0 ODs to capture the counts from the device.

The data has been taken for different comparator thresholds in attempts to find out how exactly different thresholds affect linearity characteristics.

Since our counter was designed to operate in 2 modes: 1-byte data per time interval and 3-bytes data per time interval, we needed to compare those modes too.

Figure 3.7 shows linearity curves for 4 separate cases. The graph is in log scale and we can expect that perfectly linear curve will be close to red dotted one. This way we can easily see all the deviations from linearity for different experiments.

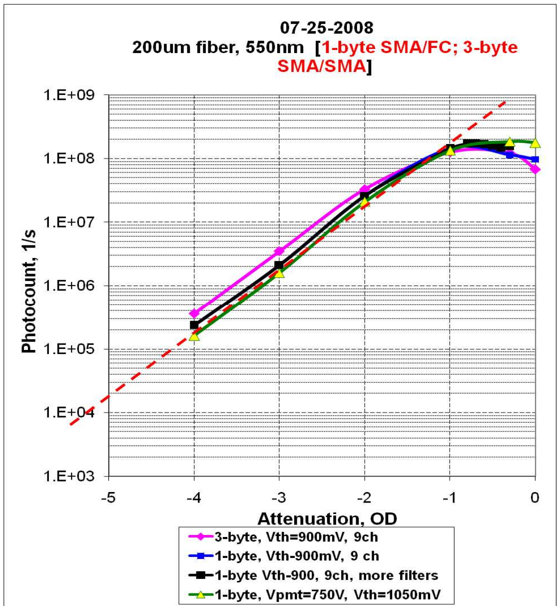

Figure 3.7 Linearity curves for 4 different counting schemes.

As it can be seen from the figure all curves are very close to each other and their behavior can be described using 3 distinct ranges of light intensity:

- From -4OD to -2OD – perfect linearity of the device. 20-30 million counts.
- From -2OD to -1OD – slight deviations from linearity, because some pulses start to appear below comparator threshold.. These deviations they can be easily corrected by post-processing. ‘sub-linear’ region. Up to 100 million counts.
- From -1OD to 0OD – Non-linear range.

The next figure (Figure 3.8) shows linearity curves for different threshold voltages. The results one more time confirm that the closer the threshold voltage is to the bottom of the pulse – the more pulses are registered – better linearity curve, until the point we start registering the noise floor. The closer we are to the noise floor while not touching it – the more linear characteristics are. Though it can be easily seen the graphs starts going down earlier, if we’re very close to the noise floor, thus putting a limit on the highest count rate.

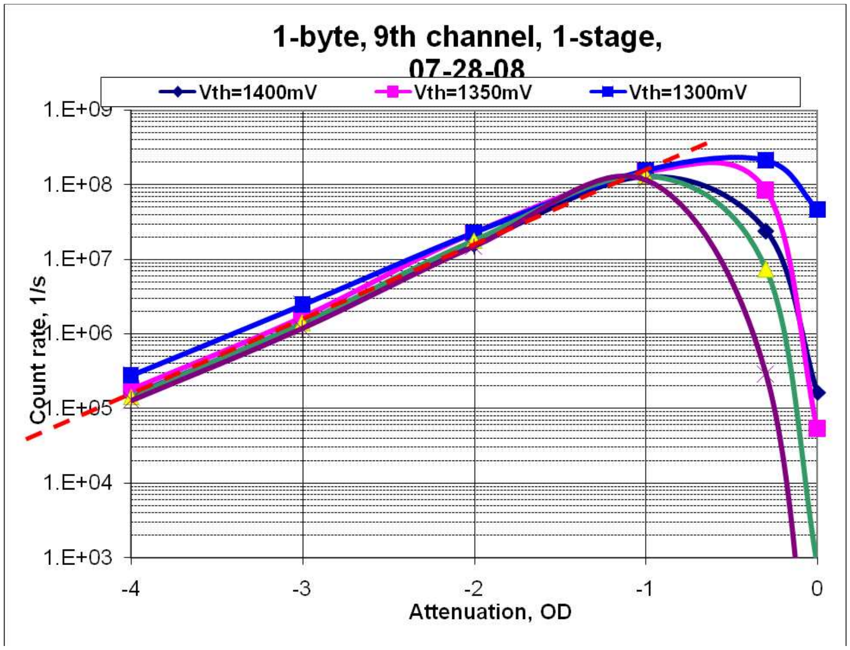

Figure 3.8 Linearity curves for different comparator thresholds.

It emperically follows from the Figure 3.8 that the threshold of 1350V is the best tradeoff between perfect linearity and highest count rate. That's why we've chosen this threshold for the following experiments.

Now our goal was to compare linearity curves for the same threshold by for different wavelengh of the incident light.

The Figure 3.9 shows 3 characteristics of 1-stage amplifier PMT counts for 3 different wavelength. For all 3 of them the output remains linear until more than 10^8 counts. Difference in absolute counts numbers for 488nm&530nm case VS 630nm is easily explained by PMT quantum efficiency characteristics, which have a peak around 450-500nm and a decreasing slope for 600+nm wavelengths.

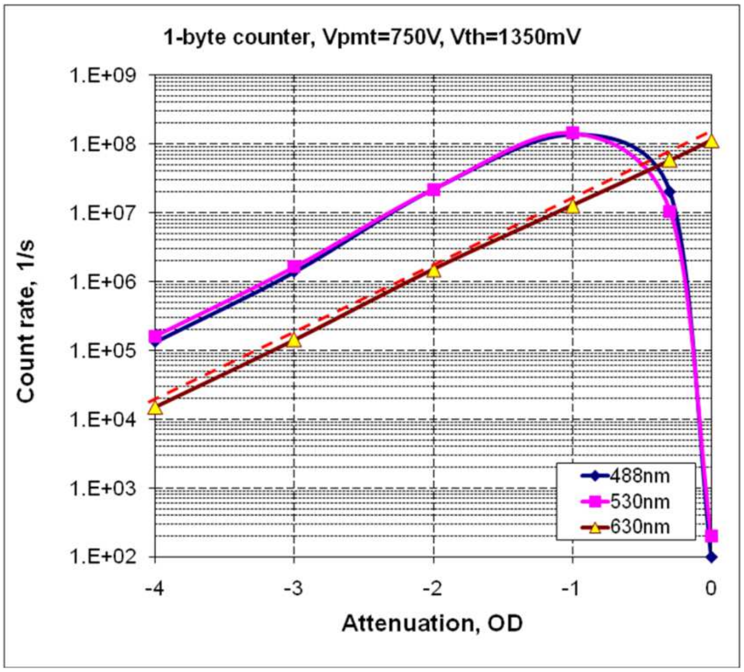

Figure 3.9 Linearity at different light wavelengh.

3.4 Crosstalk.

Next important investigation we had to perform is to measure how much the channels of our multichannel system affect each other. This is called channels crosstalk of a multichannel system. The crosstalk is an inevitable property of any kind of multichannel system when the channels are not totally separated from each other. In our case the common spots where crosstalk may occur are optical bench and its capability to focus and direct the beam of light in one single channel only and internal electronic crosstalk inside PMT or on the board itself.

Measuring channels crosstalk in multichannel PMT is very important to make corrections into all further signal measurements.

The crosstalk as it was mentioned earlier can have 2 different origins:

- Optical crosstalk, arises from illumination of a neighboring channel due to non-perfect aligning of light emitting fiber or parasitic light reflection inside the optical bench;
- Electronic crosstalk, arises from internal link between channels in PMT (amplification path is the same for all channels).

We have to note here that ‘some’ amounts of both types of crosstalk are the property of the device composition and cannot be reduced beyond some point.

To minimize optical crosstalk in our investigation we used a 532nm Ar-ion laser as the light emitter instead of the monochromator. Resulting light spot in the case of the laser will be much more confined and thus will provide much less exposure of the neighboring channels.

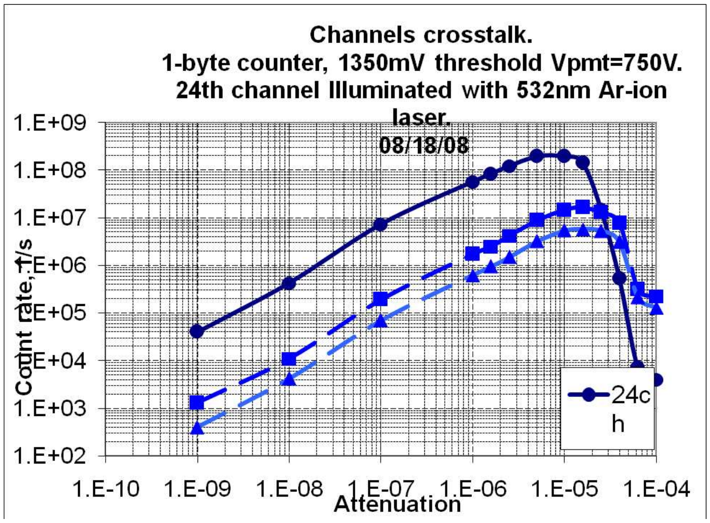

Figure 3.10 PMT channels crosstalk measurements.

What we expected to obtain is if our crosstalk is mostly optical then neighboring channels will continue to rise while the illuminated channel will get saturated and abruptly gows down. And it’s mostly electronical if the neighboring channels will follow the main channel even before they would get saturated themselves.

In the results on Figure 3.10 neighboring channels (2 lower light blue plots) are indeed following main channel pattern long before they got to 100mil cou nts. And their relative magnitude stay within 5% of the main channel which is what we expected from this type of PMT, having ~3-5% internal cross talk.

3.5 Poisson characteristics and comparator threshold.

Since the noise in photon counting system is determined by incident photons fluctuations noise we can expect that the if our system doesn’t serve as a significant source of noise the registered counts distribution will follow Poisson distribution as well.

During the course of our experiments we observed abrupt decrease of PMT pulses height and consequitive decrease in number of registered counts at high light intesities.

To find out the nature of this phenomenon we decided to proccess the counts we obtain whether they still follow the Poisson distribution for the light intensities higher the point we get the counts going down.

We used the same setup as for linearity measurements, but this time we accumulated a large number of count-per-time interval values and proccessed them. 3 different comparator thresholds (1300mV, 1350mV and 1500) have been chosen to find out which one gives us more adequate results. Lower comparator thresholds allow us to register more pulses and making our counts distribution closer to the Poisson one (presumebly the PMT pulses follow Poisson distribution), but if the threshold is too low, we would start registering noise floor. This would effectively shift our counts distribution further from Poisson.

Higher threshold as though helps us get rid of registering noise, more and more PMT pulses become lower the threshold as we pull it up and the counts will be lower.

The following set of histograms takes all counts in a large interval, then divides them into equally distances bins and plots number of events in a bin versus bins positions. This way we can expect the shape of the plots to be close to normal distribution (good approximation for Poisson when number of events is high enough) if the events follow Poisson distribution. And vice versa the shape will get more and more corrupted if the events stop follow Poisson because of pulses overlapping, threshold getting too close to the noise floor or pulses magnitude getting below fixed comparator threshold for very high light intensities as it was observed in pulses shape discussion earlier.

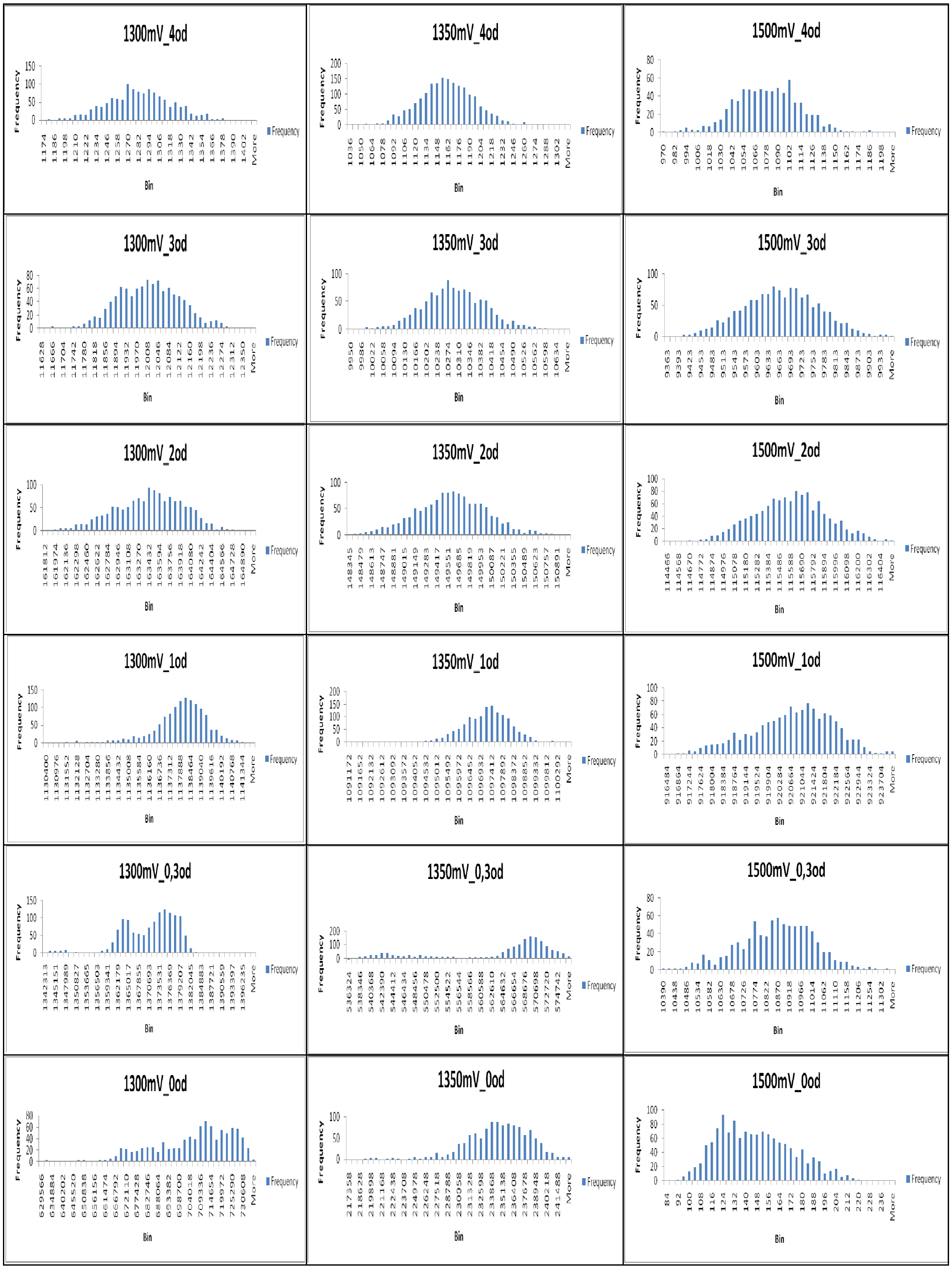

Figure 3.11 Distribution of counts at different light intensities and comparator thresholds.

As it was expected from linearity measurements the counts distribution remains close to Poisson up to 1OD attenuation But starting at 0.3OD level for 1300mV and 1350mV (which are ‘lower’ thresholds, comparing to 1500mV) the distortion gets into play and corrupts the shape of the distribution.

For 1500mV the distribution behaves slightly better, but it should have been expected as this threshold is much higher. Though even at this threshold 0.3OD and 0OD looks very different which once again tells us those light intensities are out of range of the devices performance.

CHAPTER 4

DEVELOPMENT AND APPLICATIONS OF 32-CHANNEL SPECTROMETER

4.1 Description.

In the result of the discussion we had in the previous chapter we described a working prototype of one channel photon counter. Since it proved to be a realization of our goal of having both high sensitivity and high time resolution we went on to the development of 32-channel counter device.

Since one of its major applications is supposed to be fluorescence spectrometry special type of optical head has been developed to decompose the incoming light into line spectra, as it can be seen in the figure 4.1.

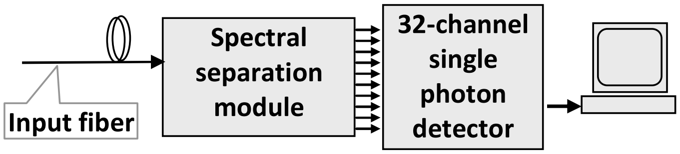

Figure 4.1 32-channel spectrometer setup.

The detector module the same as in 1-channel counter case consists of pre-amplifier circuit, discriminator circuit and counter circuit. Amplification scheme has left to be the same as in 1-channel counter case, since the amount of amplification was found to be optimal for the subsequent comparators.

This time, as a counting circuit we used one of the fastest FPGAs available at that time, namely Xilinx Virtex-5 series one. It can provide a high level of versatility onboard being able not only to count the pulses and create the output sequence into the PC, but also potentially implement some levels of DSP directly onboard. One of the key criteria in favor of the particular type of the FPGA was its high bandwidth, which is around 1.6GHz in the case of Virtex-5. Considering the fast that ~1ns pulses from PMT are getting some spread nevertheless originating from both amplifier and comparator, the pulses on the FGPA inputs have a typical width at about 2-3ns, making 1.6GHz a suitable bandwidth to be able to register the pulses of that width. Since the FPGA didn't have lvpecl inputs we swapped the comparator used in 1-channel counter to a LVDS one, with similar speed specifications.

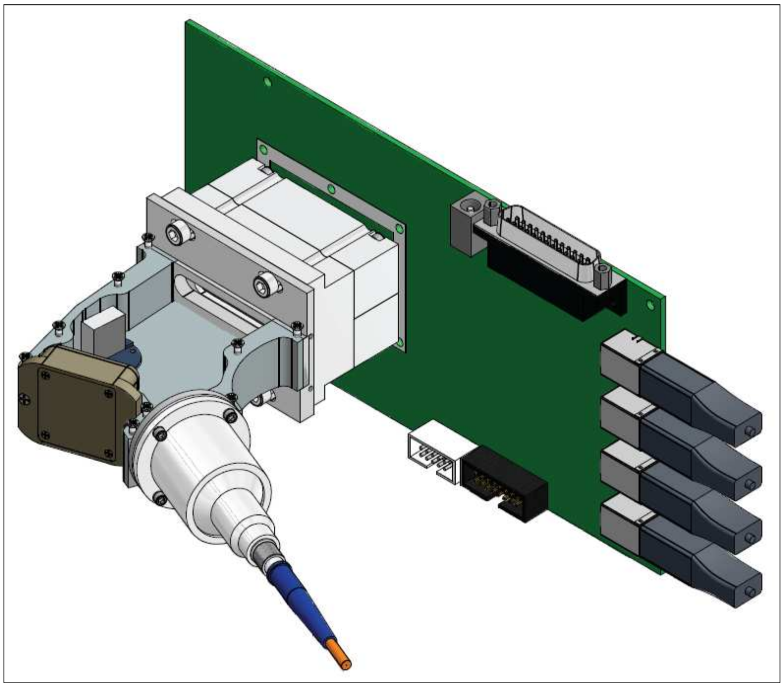

Figure 4.2 3D model of the assembled spectrometer board with attached PMT.

General looks of the device can be seen on the Figure 4.2. Unlike the 1-channel counter, the 32-channel counter has 4 USB ports as a primary means of communication with PC, thus considerably increasing the maximum data rate, comparing to LPT. Indeed, we've been able to achieve up to 1MHz counting speed per channel, totaling to up to 32MB/s overall output data rate from the whole device. Which is a large improvement over 1KHz maximum count rate of 1-channel counter. This way integration time can be brought to as low as 1usec, thus giving a very high time resolution which can be very important for many life sciences imaging applications or quantum beads detection. Data output using our custom-made software have been proven to be stable and error-free at the maximum speed over ~10 hours continuous recording.

Top view on the 32-channels counter board is provided on Figure 4.3. PMT is mounted on the center part of the board. The amplification circuits and comparators had to be situated as close to the PMT outputs as possible to prevent unnecessary signals distortion. All analogue parts are physically separated from digital ones, to reduce influences. FPGA governs all digital processing and a separate Cypress CY7C68013A usb-controller performs all communication with PC over USB output.

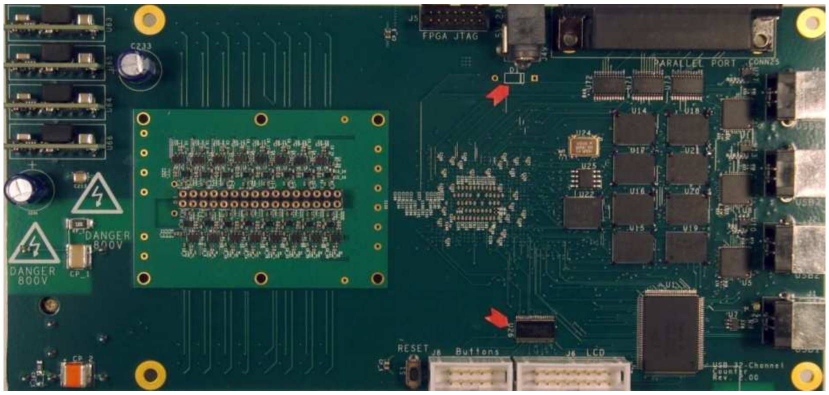

Figure 4.3 Top view on 32-channel spectrometer PCB.

LPT output is also supported and can be used when measuring slower changing signals. General looks of the assembled device in its box can be seen at Figure 4.4.

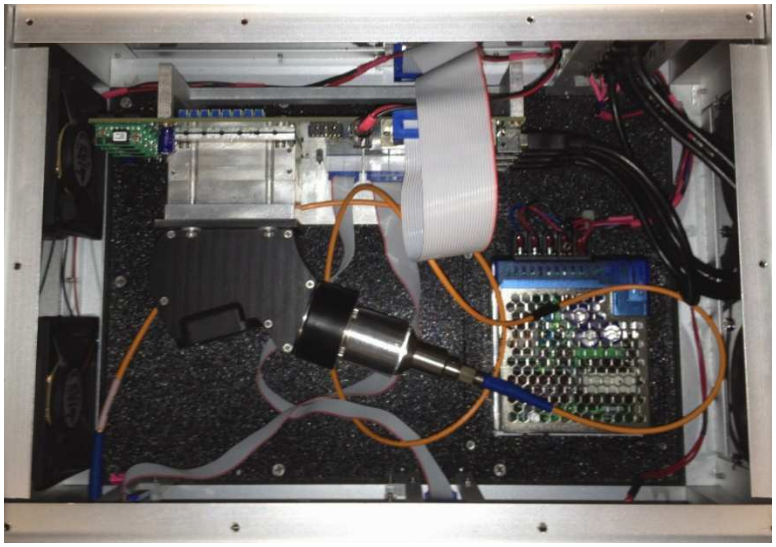

Figure 4.4 Top view on the spectrometer in the box.

It's a top view, with the board with attached PMT in the center-left part. Lower-right part has the 5V power supply for the whole device and the fiber connecting spectrometer with the SMA jack on the outer side of the box.

Frontal panel on the Figure 4.5 has a display and control buttons which allows us to choose data modes the device is capable to work. Possible modes include a choice of each of its 4 USB outputs, LPT output mode and different framerate settings for every output.

```
32-Channel Counter     Rev.01.50.10
Port: USB 1         Status: Not Ready
Frame Format: Format 1
Data Rate: 10^6Hz
Run Control:          Status: Stopped
Current Frame Number:  000000000000
Sent Frames Count:     000000000000
Dropped Frames Count:  000000000000
```

Figure 4.5 Frontal panel of the 32-spectrometer.

4.2 Spectral separation module (optical head).

Since compared to the single channel counter now the light has to be guided into a linear array of 32 channels we developed a special optical head specifically designed to accommodate spectrometric experiments.

As it can be seen on Figure 4.6 the optical head consists of fiber input with a filters holder space and the optical bench. The whole construction firmly attached to the front of PMT case.

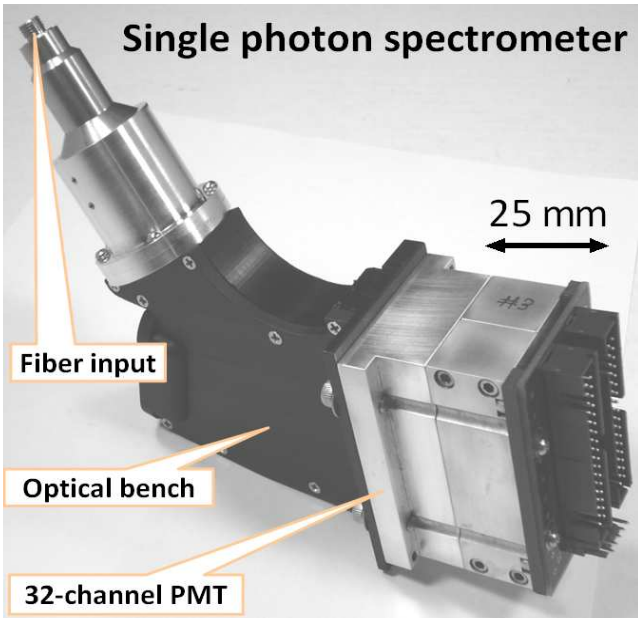

Figure 4.6 Photo of optical head for 32-channel spectrometer.

The spectral separation module performs the separation and the measurement of light in the range of wavelengths from 480nm to 670nm. The light is brought into the spectrometer through the input fiber coupled to the collimator (F810SMA-543, Thorlabs Inc, NJ, USA) which produces a parallel polychromatic beam of ~10mm diameter.

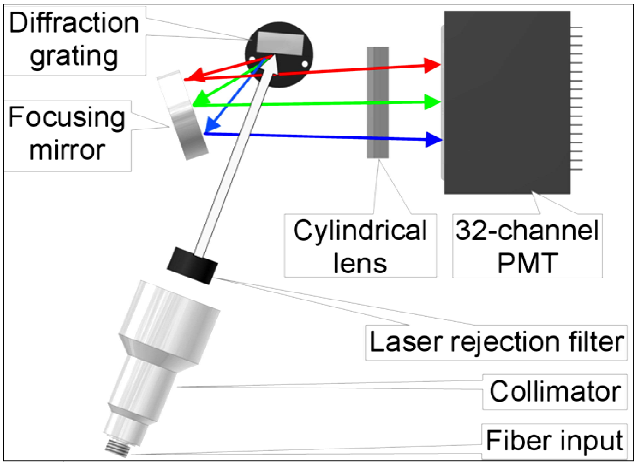

Figure 4.7 Light propagation through the optical head.

The parallel beam passes through laser rejection filters and undergoes separation on the diffraction grating (GR13-1850, Thorlabs Inc, NJ, USA) into constituent wavelength components (Figure 4.7). The separated monochromatic beams are focused onto channels of the 32-channel PMT (H7260-20, Hamamatsu, Japan) by the system comprising spherical mirror (CM254-075-G01, Thorlabs Inc, NJ, USA) and cylindrical lens (LJ1095L2, Thorlabs Inc, NJ, USA).

4.3 Pulse shapes.

Since we're using a different comparator with different output signaling (lvds vs lvpecl) we can expect to have a different pulse shapes on its output. The Figure 4.8 represents pulses after PMT on the left and pulses after the comparator on the right.

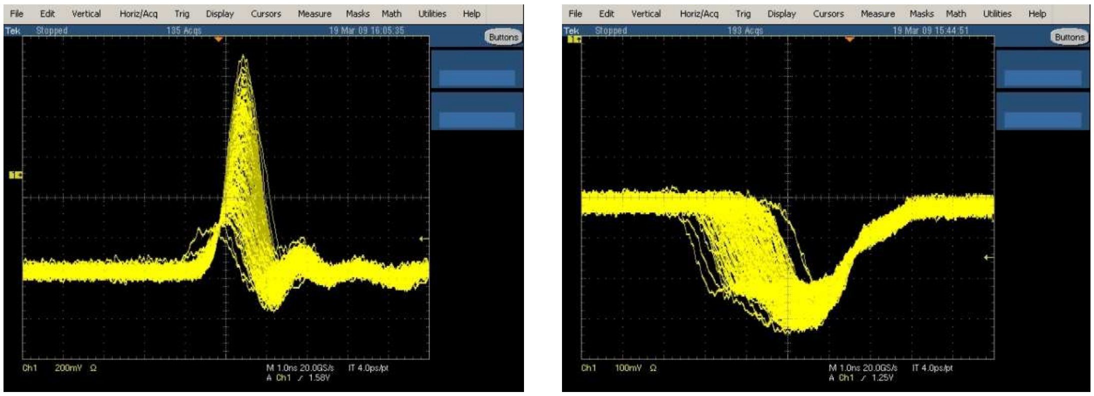

Figure 4.8 Pulses after PMT (left) and comparator (right) in 32-channel spectrometer.

We have to note, that comparator pulses though being <4ns with average about 2.5ns are good suited for photon counting purposes LVPECL comparator had slightly better timing characteristics. Though a slight hit onto linearity characteristics comparing to single channel case could be expected and was indeed observed in the discussion in the following chapter.

4.4 32-channel spectrometer linearity.

As well as in the case of single channel counter we performed extensive measurements of the linearity of all 32 channels of the device. Test setup (on Figure 4.9) was very similar to the single channel case.

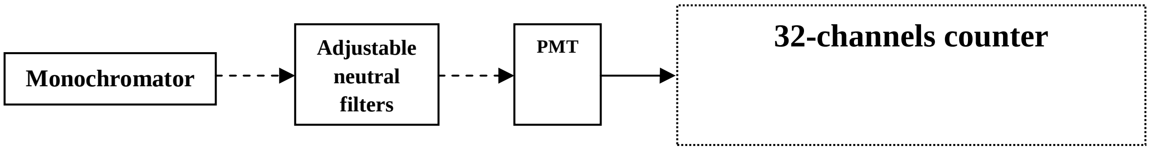

Figure 4.9 Multichannel linearity measurements setup.

We used the same single channel PMT header and focused it on each channel in turns. One arbitrary chosen channel result is shown on Figure 4.10 and multichannel results on Figure 4.11.

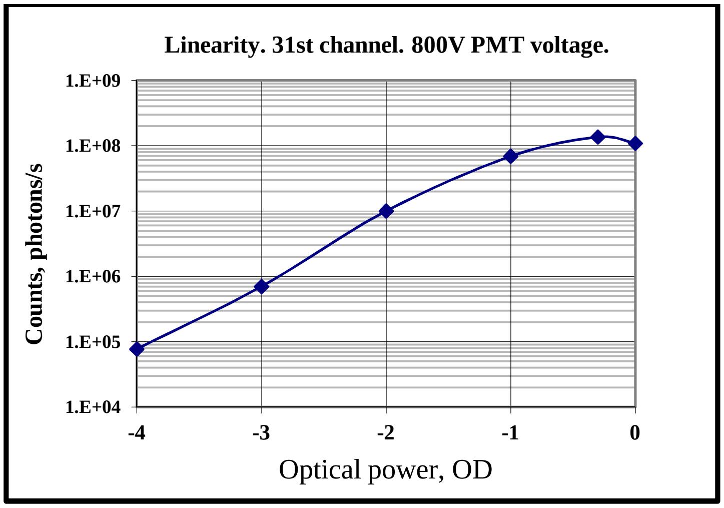

Figure 4.10 Single channel linearity curve.

As we can see on the graph, the linearity of the 32-channer counter is slightly worse than in case of single channel counter mostly due to different comporators used.

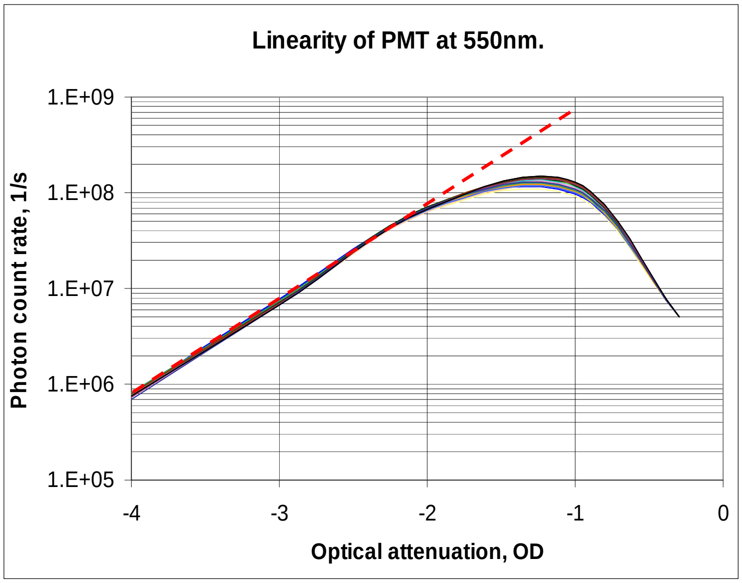

Figure 4.11 Multichannel combined linearity curves.

Another reason for the notable difference in linearity curves arose due to the fact we had to move comparators's thresholds oven further from the noise floor as different abmient conditions may and have resulted in slight variation in setup performance resulting in thresholds occasional touching the noise floor if there are too close to each other. Nevertheless despite the fact that we made considerable changes into the components of the device the performance ended up to be only slightly worse than in our prototype single channel case and almost perfect linearity was achieved up to 60-70 millions counts per second. With correctabale by post-processing linearity reaching 100-110 millions counts per second.

4.5 Spectral characteristics.

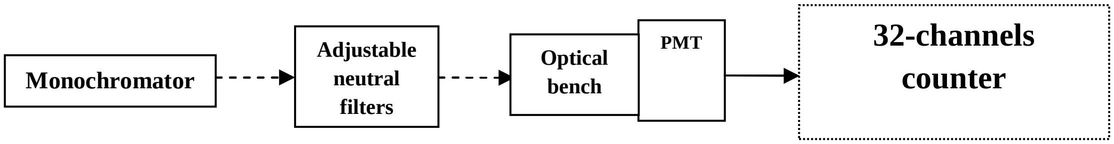

Figure 4.12 Spectral characteristics measurements setup.

In order to take spectral characteristics of the whole 32-channel device we used a modified setup (Figure 4.12) comparing to linearity measurements. Monochromator is used to gradually alter the incoming light’s wavelength from 520nm to 740nm. This way each channel will have a different wavelength on it and if we will do continuous recording from all the channels we will be able to plot spectral response of the whole device.

In order to characterize the spectral separation module we connected the input fiber of the spectrometer to a monochromator. We found that the wavelength resolution of the sensor is ~10nm per channel. Analysis of the spectral separation module of the spectrometer shows that it can provide spectral resolution as high as 1nm. The obtained spectral resolution of ~10nm is determined by the geometry of the 32-channel PMT which comprises 0.8mm×7mm detection zones separated by 0.2mm distance. The overall resolution of the sensor can be improved by using an array of photo receiving fibers connected to single photon sensors.

Below (Figure 4.13) are the typical spectral response plots from the 32-channels counter in linear region:

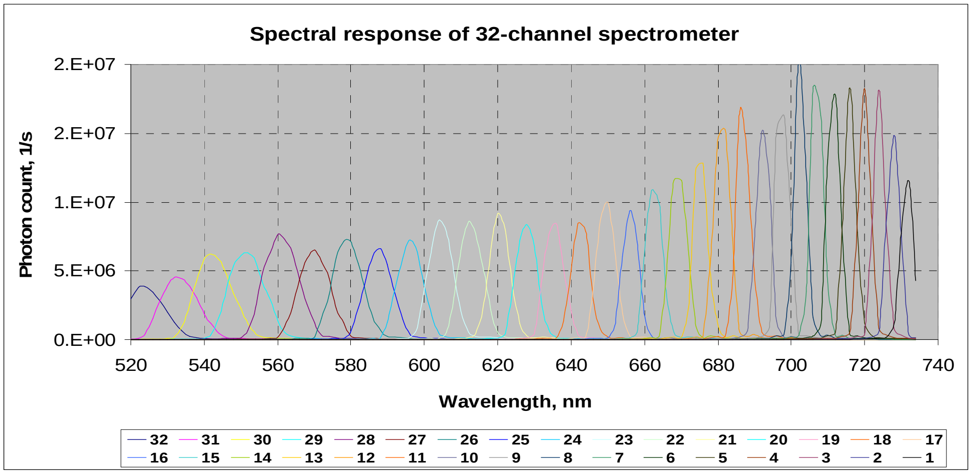

Figure 4.13 32-channels spectrometer spectral response in 520-740nm range.

As seen on Figure 4.13 each channel has a wavelength with uniquely corresponds to this channel with this setup of the spectrometer. That's why we can do a reverse plot of intensity vs. channel number instead of wavelength and get a similar type of plot (Figure 4.14)

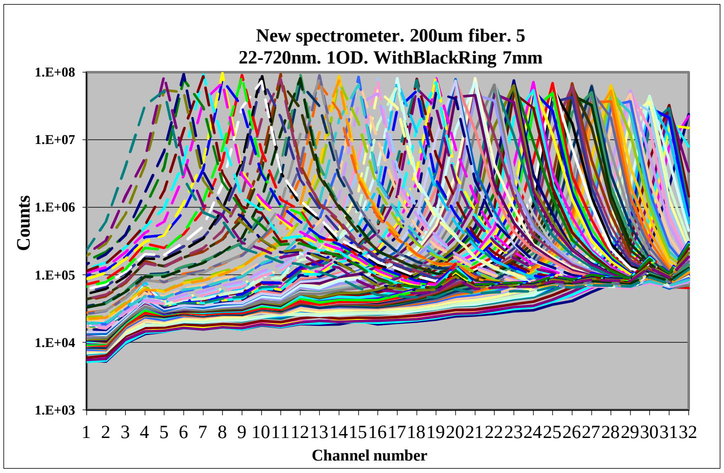

Figure 4.14 Counts vs. channel number spectral response plot.

We’re able to ‘shift’ the whole wavelength picture by either rotation the diffraction grating inside the optical bench or by shifting optical bench along the front of the PMT case. Both ways combined we can cover the range from ~450nm up to 800nm with this device.

4.6 Dark counts and noise.

The noise in the photon counting system is determined by the temporal distribution of photo-counts. In a correctly operating photon counter we observe Poisson distribution of the photocounts for which the variance of the photo-count rate estimate is equal to its mean value, setting the lower boundary for the signal-to-noise ratio of the photon detector. In order to determine the distribution of photocounts in our detector, we collected photocounts during 25ms intervals for different light levels and recorded using our data recording software for ~30 min (Figure 4.15). The obtained good match between mean values and variances for all illumination levels indicate that the measured noise is only caused by the stochastic nature of the photon fluxes detected by the detector and that the detector itself does not produce any additional noise.

As it’s expected the results are quite similar to single channel counter noise discussion in previous chapters.

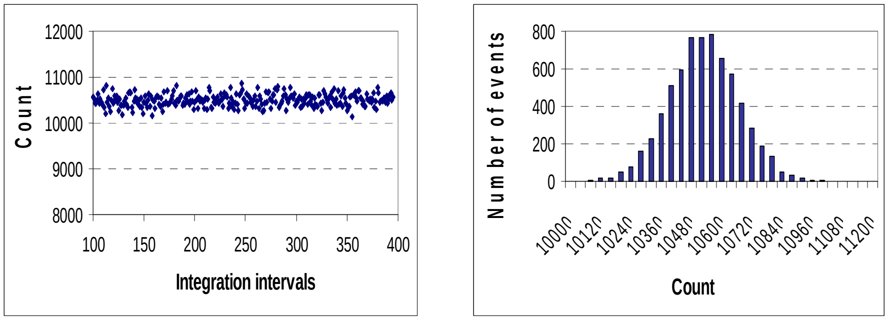

Figure 4.15 Counts distribution in 32-channel spectrometer output.

As we're using a different comparator in 32-channel counter opposed to single channel counter case we performed additional investigations of valid threshold level and obtained the plot on Figure 4.16.

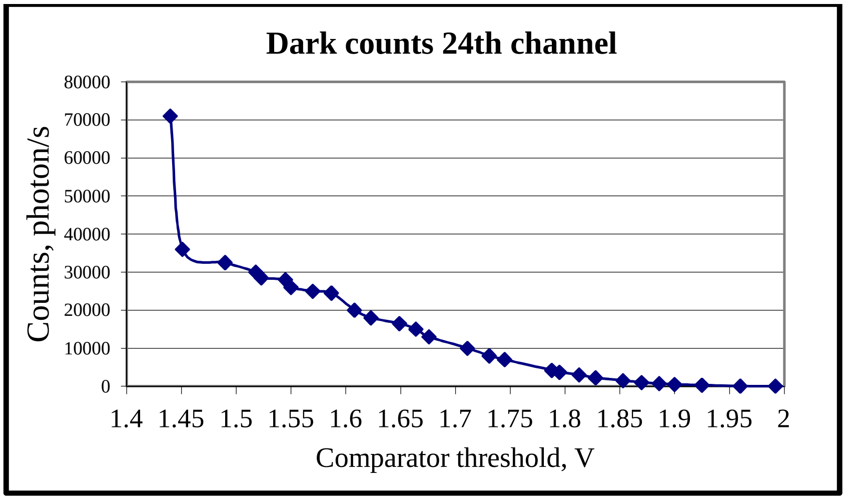

Figure 4.16 Dark counts relation on comparator thresholds.

It can be seen that any threshold value between 1.45 and 1.55V is suitable for comparators' threshold though due to channels non-uniformity exact figures has to be determined individually for each channel.

4.7 Measurements of quantum dots mixtures using 32-channel spectrometer.

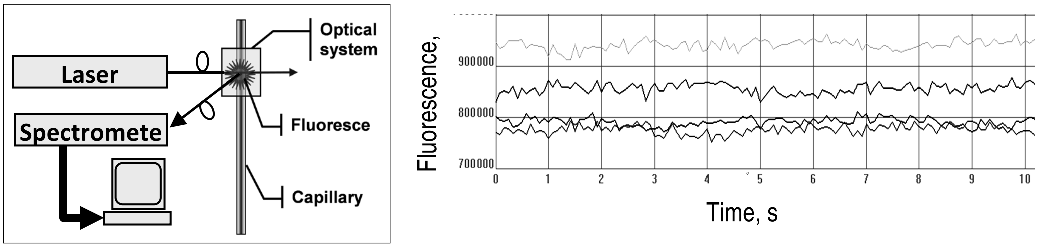

Figure 4.17 Schematic of the measurement setup (left) and typical fluorescent signal from solution of QDs in toluene recorded in four channels of the spectrometer during 10 seconds (right).

Block diagram of the setup for measurements of fluorescence spectra is shown in Figure 4.17. In the setup, a substance to be analyzed is placed in a capillary which is inserted into a fiberized optical system (see [9] for detailed description of the optical system). Fluorescence in the analyte is excited by Ar-ion laser (488 and 514nm, Uniphase, CA, USA), collected by the fiber (200mkm core diameter) and delivered to the spectral separation module. Detection of the capillary content may be done by either pulling the capillary through the optical head using a programmable stepper motor or pumping the analyte through the capillary using a programmable micro-pump.

In order to test the proposed method for detection and recognition of mixtures of quantum dots as well as the developed software for simulation of the single photon spectrometer, we have carried out measurements of mixtures of three different types of QDs with strong spectral overlap (Figure 4.17). QDs re-suspended in toluene 1mg/ml were obtained from Crystalplex Inc, Pittsburgh, PA.

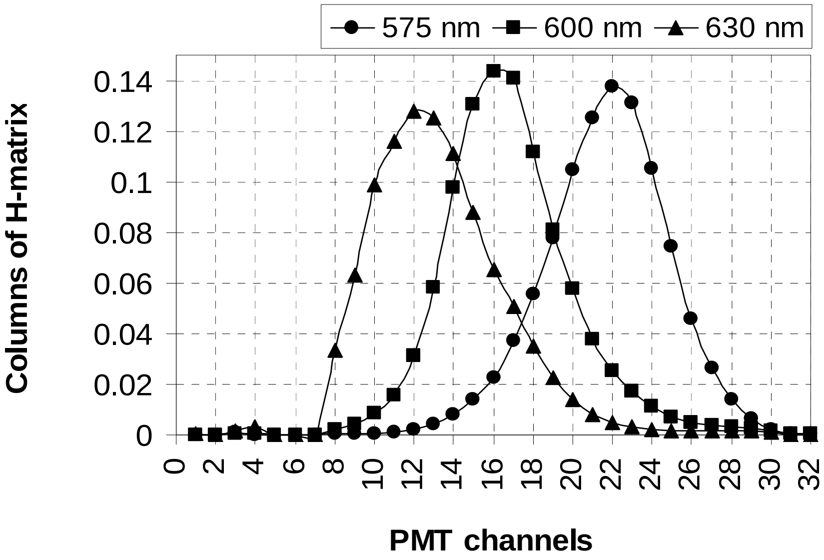

Figure 4.18 Spectra of individual quantum dots.

We premixed 50% of 575 nm QDs and 50% of 630nm QDs and prepared a series of mixtures in which the content of 600nm QDs varied from 0% to 15%. Mixtures of quantum dots were placed into fused silica capillaries with transparent coating (360um OD, 100um ID, Polymicro, AZ, USA. The total recording time for each mixture was about 5 minutes with minimum integration time of ~20ms which provided approximately 15,000 data points per mixture. The color deconvolution procedure described in Section 2 was applied to photocounts obtained in 32 channels at each data point during 20ms photon integration time. In order to increase the photon integration time, we added photocounts obtained from several sequential data points and thus applied the color deconvolution procedure to longer time intervals.

Based on the measured spectra of individual QDs we have determined the **H**-matrix and carried out color deconvolution procedure. The obtained results are presented in Figures 4.18 and 4.19.

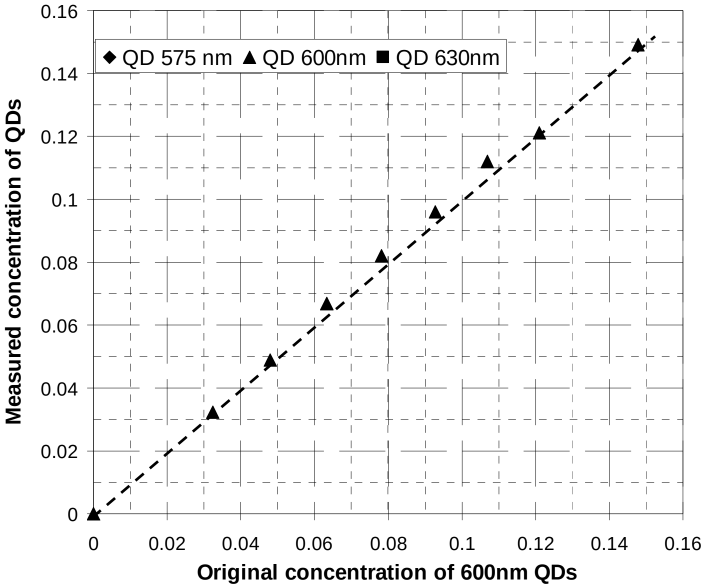

Figure 4.19 Concentration of QD 600nm determined experimentally versus concentration of this dye in the prepared dye mixtures.

As can be seen from Figure 4.18, the concentration of the 600nm QDs determined from the fluorescence measurements is practically equal to the original concentration of this dye in the prepared dye mixtures.

Figure 4.19 presents distribution of concentration of the 600nm QDs recovered from multiple measurements of the dye mixtures with 0.1s and 0.02s integration times.

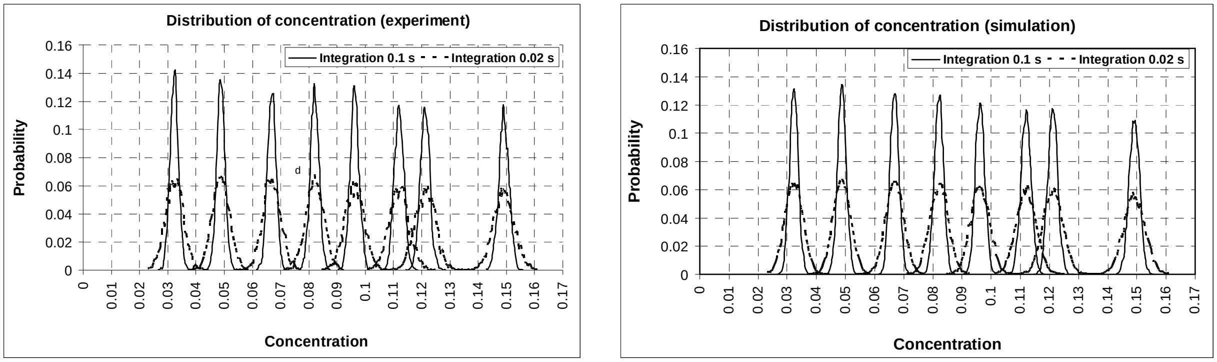

Figure 4.20 Distributions of concentrations of 600nm QD determined with 0.1s and 0.02s integration times (experiment-left panel, and simulation-right panel).

As can be seen, increase of the integration time improves the resolution of dye mixtures. Comparison of distributions of dye compositions obtained experimentally and in by the simulation shows an extremely good agreement. Based on this we conclude that the developed simulation tool can be used for prediction of the accuracy in detection and recognition of dye mixtures.

CHAPTER 5

RECOGNITION AND CORRECTION OF NON-LINEAR MEASUMENTS IN DETECTION OF INIVIDIAUL MULTI-COLOR FLUORESCENT OBJECTS

5.1 Introduction.

In this chapter I proposed a new method to detect and correct non-linearity in multichannel photon counter devices. The method requires excessive number of spectral channels compared to minimum number (which is equal to the number of fluorescent dyes).

Linearity of fluorescent detection is necessary for accurate color de-convolution. The question is how to ensure that measurements of fluorescent objects by photon detector are performed in linear mode.

Each photon counting device has the upper bound of its dynamic range. If photon counts are too high device goes into saturation (Figure 5.1) and starts providing less and less counts for increased light intensity on its inputs. In case of our detector we have the following characteristic:

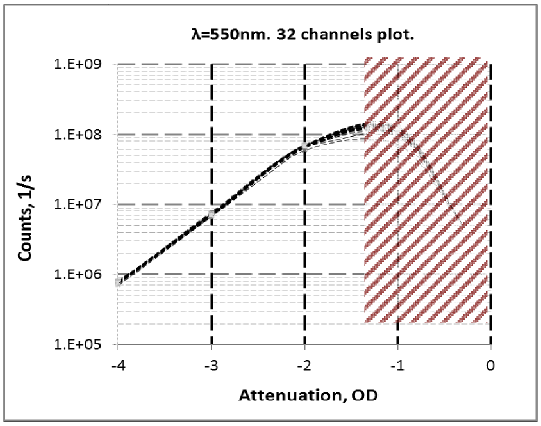

Figure 5.1 Saturation region in the linearity plot.

Here the counts stay linear up to 5x10^7 photo-counts/sec, then their behavior starts to deviate from linear mode and finally at about 1.1x10^8 photo-counts/s the counts abruptly drop.

There are two major reasons for nonlinearity and decrease of photon count at high illumination level:

1. Statistically, photon counts have poisson distribution of inter-count distances. When time distance between consecutive photon pulses becomes smaller than Full Width Half Maximum of current pulses generated by individual photons, the consecutive photon pulses are counted by the photon counter as a single pulse, reducing measured photon count compared to the true count;
2. Another reason is reduction of the amplitude of current pulses generated by single photons (see Figure 3.3). In this case it becomes very difficult to separate dark counts from photon generated counts. In other word, it becomes impossible to determine threshold photon count for separation of photon counts from the dark noise. In fact, time distances between dark pulses and photon pulses become too small, and photon counter counts series of dark and photon pulses as individual single pulses which reduces total photon count at too high illumination level.

Even though 5x10^7 count/s is a very high number for photon counting the beads may go through the laser beam very fast (100us aren't an unusual figure) so our linearity range allows as to capture about 5000 photons per bead. This threshold can be broken quite easily since during one experiment we have beads with quite different light and some of them may be deep into non-linear mode.

Major problem here is that at high intensities we can't reliably tell looking at the counts if the bead is in linear mode or deeply non-linear since the counts may be the same.

To alleviate this problem we developed a non-linearity detection and correction technique.

5.2 Bead processing algorithm.

Currently beads detection and processing works as follows: the high speed fluorescence detection system is recording the number of photons received in each channel of 32-channel PMT during each sampling period. PMT channels represent wavelengths from the set range. Each bead travelling across observation window is visible on the traces in several channels as a peak. Width of the peak depends on the velocities of the beads. A number of preprocessing steps is applied to the raw data in order to extract information on individual beads:

- Background fluorescence is estimated in each channel and subtracted from the respective trace.
- Peak detection is performed using the sum of all 32 traces. Position and width of each peak is estimated. Each peak represents individual bead passing across the observation window.
- Calculation of total number of photons received from each bead. The total number of photons is computed in each data channel by integration of the respective trace over each detected peak. Peak width is used to find the beginning and the end of the integration period. The result of this step is fluorescence spectrum $\mathbf{f} = \left(f_1, f_2 \ldots f_{32} \right)^T$ of each detected bead.
- Detection of the maximum photocount density in each channel for each bead. The maximum photocount density in the sampling interval closest to the top of the peak is saved as $\mathbf{f}^{\max} = \left(f_1^{\max}, f_2^{\max} \ldots f_{32}^{\max} \right)$.

The purpose of the processing is estimation of contribution of each of n dye marker $\mathbf{x} = \left(x_1, x_2 \ldots x_n \right)^T$ to the fluorescence spectrum of each bead $\mathbf{f}$. Spectra of dye markers are measured during calibration. The spectra are normalized and recorded as columns of the matrix $\mathbf{H} = \left(\mathbf{h}_1, \mathbf{h}_2 \ldots \mathbf{h}_n \right)$, where $\mathbf{h}_k = \left(h_{k1}, h_{k2} \ldots h_{k32} \right)^T$ and $\sum_{i=1}^{32} h_{ki} = 1$. Values of $\mathbf{x}$ can be obtained by solving the equation

$$\mathbf{f} = \mathbf{Hx} \tag{5}$$

for each bead. The problem can be simplified by assuming that noise in all the channels is Gaussian independent, and identically distributed. Then simple optimal solution of the Eq.(5) using maximum likelihood method exists [11]:

$$\hat{\mathbf{x}} = \left(\mathbf{H}^T\mathbf{H}\right)^{-1}\mathbf{H}^T\mathbf{f}\ . \tag{6}$$

This method works very well if nonlinearity of the photodetector is relatively small, which is true for beads with weak fluorescence, but may fail if a bead with strong fluorescence is encountered and the signal in some PMT channels falls out of linearity range of PMT. The following approach is used in order to sort out the channels with excessive level of fluorescence:

- Select photocount rate threshold f_{th} that sets the top of linearity range of the PMT.
- For each detected bead start with full matrix $\mathbf{H}$ and fluorescence spectrum $\mathbf{f}$. Compare each element of $\mathbf{f}_{\max}$ with f_{th}. If $f_k^{\max} > f_{\text{th}}$ then exclude k-th row from $\mathbf{H}$ and k-th element from $\mathbf{f}$.
- Normalize each column of the modified $\mathbf{H}$. Compute the estimate of $\mathbf{x}$ using Eq.(6).

This way we can sort out channels with higher levels of light and after some number of iterations we can expect approach the situation where only linear channels are left. Each time we obtain a sequence of normalized beads spectra (bead codes) and we can expect that most of the spectra for the same type of beads will be very close to each other. And this ‘spread’ of the spectra won’t change while we dropping channels.

5.3 Results of non-linearity correction.

To test our algorithm we used sets of differently colored Luminex beads. Then we recorded the beads going through the capillary at different intensities of the laser (marked 70mW laser or full laser and 1OD – 10 times lower). Our expectations were that for 1OD case most if not all the beads will be in linear mode. This way we had an excellent way to compare if dropping channels from full laser recordings (expected to be non-linear at some beads) will give us the same bead code as linear recordings.

Both beads type I present here (#61 and #92) have 715nm peak wavelength. The only difference is #61 has slightly less fluorescent dye.

For Luminex beads #92 the spectra of the beads are presented on Figure 5.2.

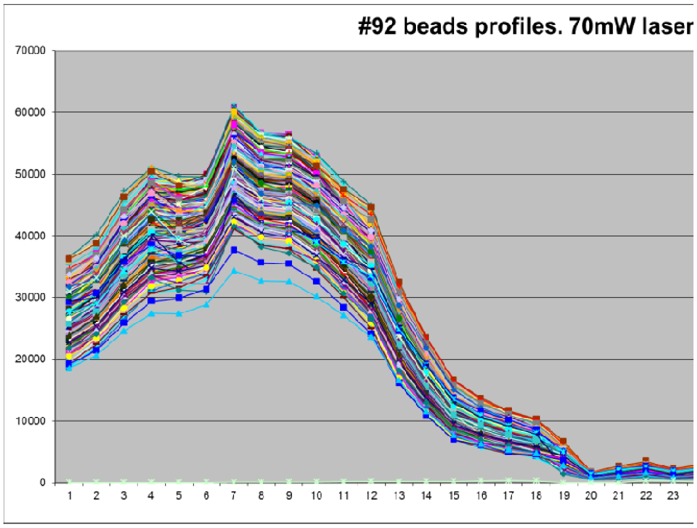

Figure 5.2 Beads #92 spectra.

As we can see the dye respond is in between 1-20 channels, so we can predict that dropping more than 20 channels will give us incorrect results.

On Figure 5.3 there's a plot of bead code versus number of channels dropped. We can see that at N(-0) – no channels dropped, original code – there's a big spread of code values between each beads. From 0.9 to 0.94. But as we drop more and more channels the spread gets narrower until it stabilize at about 0.98-0.99. As we predicted after N(-20) there's no reliable data.

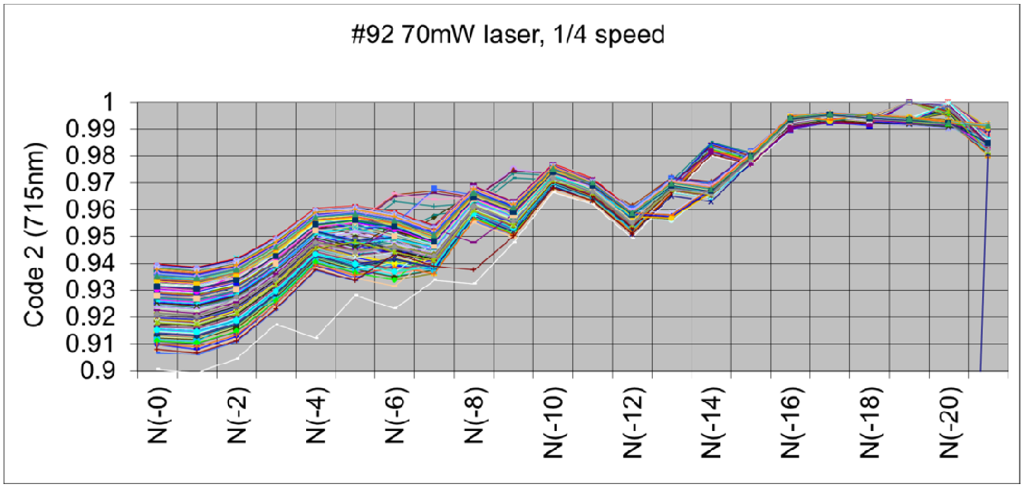

Figure 5.3 Beads #92, code versus dropped channels. Full laser.

Now on Figure 5.4 we have the same plot, but for 1OD laser intensity. We can observe that until N(-18) it is quite stable and the value of the code is 0.98-0.99 – same as we obtained in full laser case after dropping 16-20 channels.

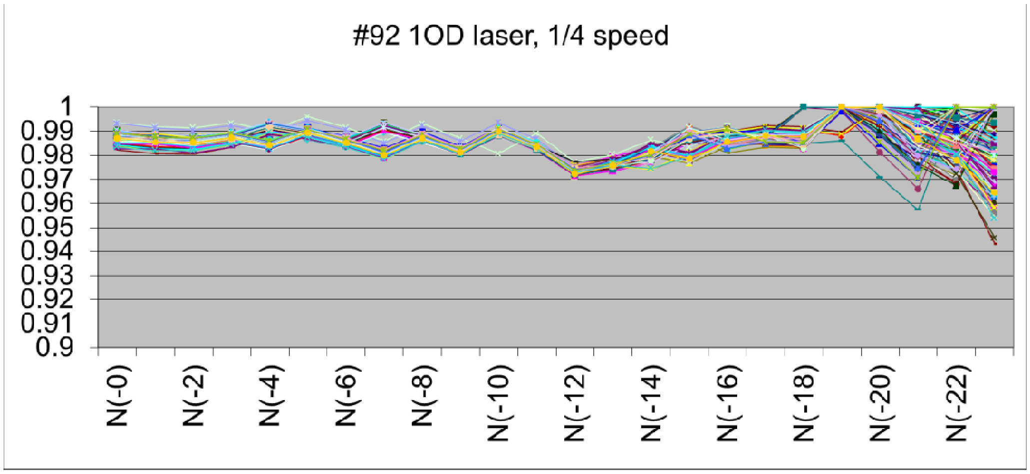

Figure 5.4 Beads #92, code versus dropped channels. 1OD laser.

Next we examine #61 Luminex beads case. Figure 5.5 has theirs spectra. As expected it is almost the same as in #92 case, but intensities are slightly lower.

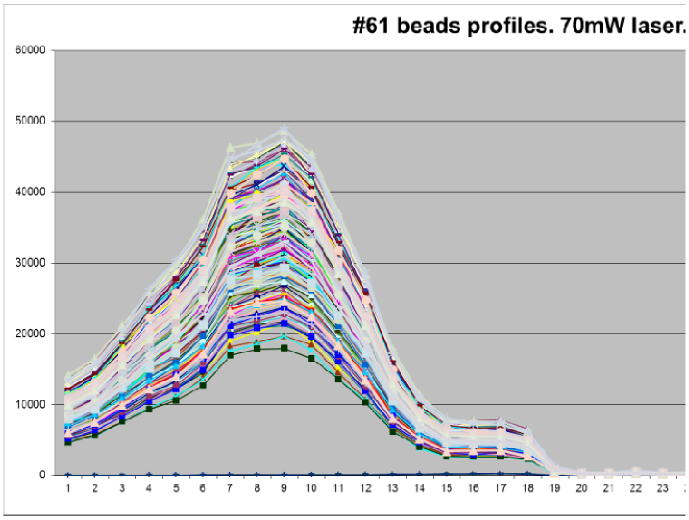

Figure 5.5 Beads #61 spectra.

For the full laser case (Figure 5.6) we observed that bead code value stabilized at about N(-10) step at 0.95-0.96 value. We can see that channels 14-20 slope is lower than in#92 case, thus inconsistent values of the codes in N(-13)-N(-20) range.

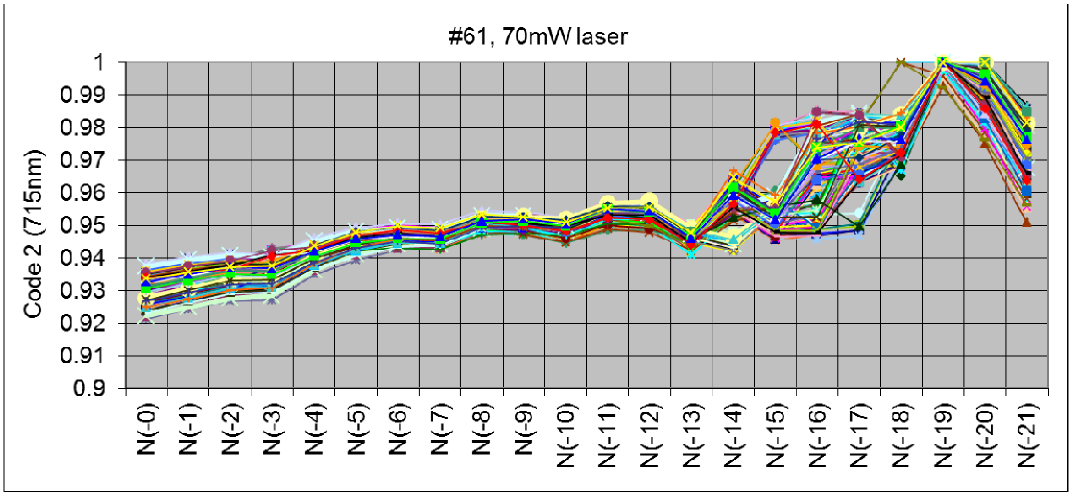

Figure 5.6 Beads #61, code versus dropped channels. Full laser.

And in 1OD laser case (Figure 5.7) the spread is again quite stable at 0.94-0.96 codes range.

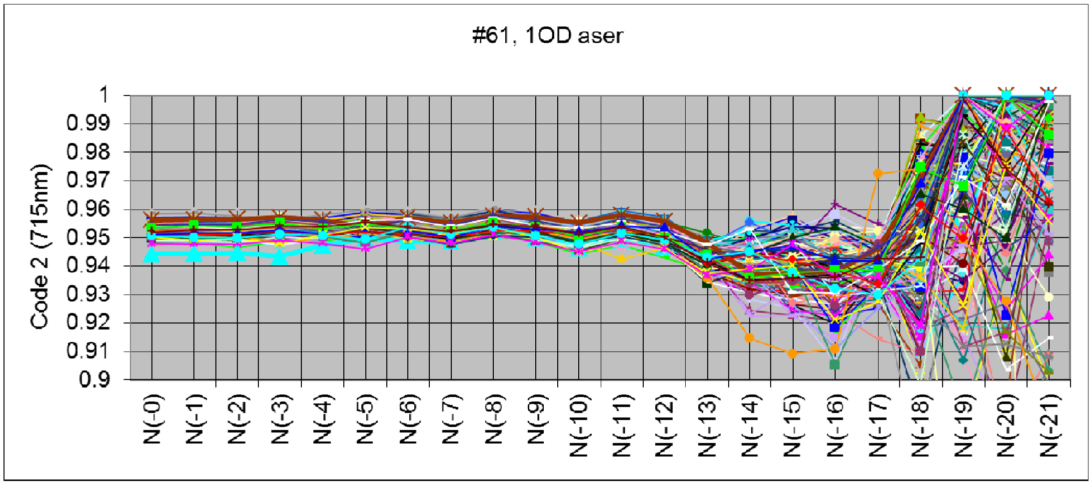

Figure 5.7 Beads #61, code versus dropped channels. 1OD laser.

Thus, we proposed a new method to detect and correct non-linearities in multichannel photon counting devices. A slight shortcoming in implementation may be that we need to have more channels in the detector than the number of dyes we try to detect.

5.4 Conclusion.

Judging from our investigations for the method to be reliable and effective in **detecting** if particular measurement was linear or non-linear we need to have at least 2-3 extra channels in the range of the dye – to detect a slope of codes versus number of dropped channels plot.

For **correcting** non-linearities and obtaining the true value of the bead code, apparently we need to have at least 10 extra channels of the detector.

One of major advantages of the new method is that linearity data and even non-linearity correction can obtained from the same measurement, though it’s important to note that at least some of the channels have to be linear to obtain reliable information about non-linear channels.

Nevertheless for many multipurpose detectors in a wide variety of applications the extra channels can dramatically improve precision of beads code detection, comparing to the case of 1 channel – 1 bead.

CHAPTER 6.

GENERAL SORTING PRINCIPLE FOR FLUORESCENT ACTIVATED SORTING.

6.1 Introduction.

Sorting of micro-objects is a widely used method in many life sciences applications. One of the benefits of this approach is the ability to streamline the detection and separation of different biological samples based on the fluorescent markers on them.

Currently almost all methods to sort the particles in the capillary require additional containers for the particles, usual in a form of bubbles of liquid [12,13] or high voltage equipment to magnetize a set of beads and perform sorting using high voltage electrodes [14,15]. Apparently there's no effective way of sorting 'bare' non-charged micro-particles. Currently there's only one work involving mechanical valves as means for sorting of micro-particles [16].

There exist multiple solutions for sorting micro-particles for different applications. The goal of this particular research is to improve the efficiency of CNV detection and other types of tasks requiring to detect and sort relatively small percentage of events (~1%), while having a high detection throughput (~10000 events per second).

Copy-number variations (***CNVs***) are alterations of the DNA that results in the cell having a normal variation in the number of copies of one or more sections of the DNA. CNVs correspond to relatively large regions of the genome that are presented in fewer or larger number than normal on certain chromosomes. This variation accounts for roughly 1% of human genomic DNA and each variation may range from about one 1,000 bases to several mega-bases.

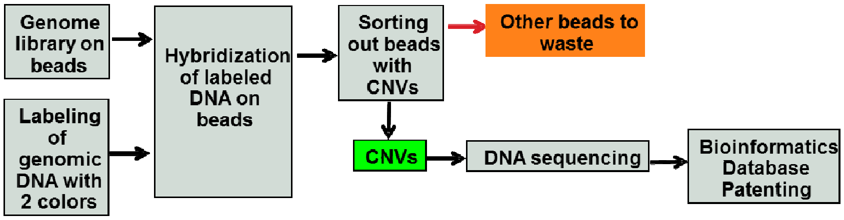

Figure 6.1 CNV sorting method.

<u>Our CNV detection technology includes the following steps:</u>

A. Generation of water-oil emulsion with droplets containing beads and single fragments of cut genomic DNA (This step is performed using microfluidic chip)

B. Preparation of whole-genome templated library on beads by emulsion PCR

C. Hybridization of fluorescence-labeled genomic DNA from control and patient on the bead library

D. Fluorescence activated sorting of the beads which show ratiometric changes corresponding to CNVs.

E. Sequencing of DNA hybridized to the beads which carry CNVs, and creation of CNV data-base.

Our bead sorting technique described in this chapter can serve as an alternative to the currently most widespread Comparative Hybridization Arrays (CGH) based method and can reduce the price for genome analysis from ~$1000/per genome down to ~$100.

In order to sort the beads we run them through the capillary with T-junction (Figure 6.2).

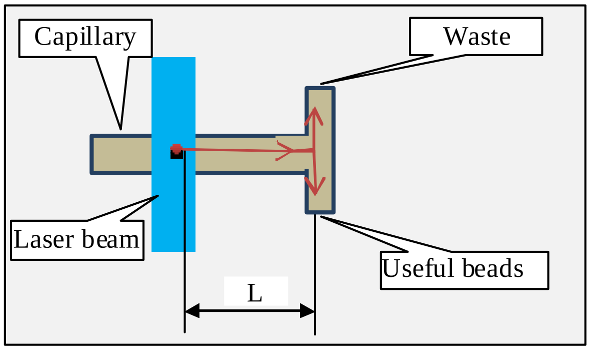

Figure 6.2 Bead in capillary channel.

Laser beam illuminates the capillary and when the bead crosses the laser beam it produces fluorescence. The fluorescence is directed to multi-channel photon detector so that different channels of the detector receive different ranges of fluorescent spectrum of the bead (Figure 6.3).

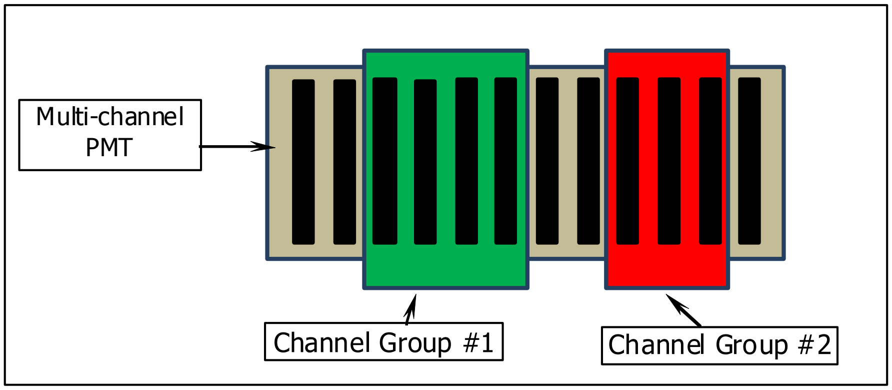

Figure 6.3 Front view of multichannel detector.

Depending on the ratio of photon counts in the two groups of channels (**R**) we can distinguish beads which we want to select (sort) from the beads which go to waste. And when the sorting event takes place we send the control signal to open the valve in the sorting branch of the T-junction.

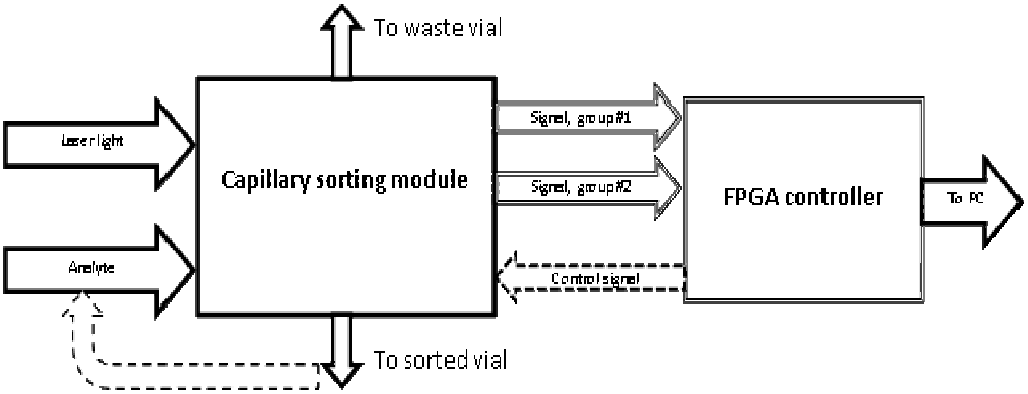

Figure 6.4 Block diagram of the sorting system.

On Figure 6.4 we have a schematic diagram of the sorting system. The main block "Capillary sorting module" consists of a pressure pump, set of the capillaries, a sorting valve, an optical head with laser input and a PMT sensor. Provided with laser light and analyte (mixture of beads to sort) it outputs signal from channel groups 1 and 2 for integration, counting and comparison in the FPGA unit. FPGA outputs the control signal to the valve when the sorted bead event is detected.

Beads from the sorted vial are fed back into the input of the capillary sorting module for subsequent sorting cycles until the desired sorted efficiency limit is met.

Compared to other widespread particle sorting technique using a FACS machine our valve-based sorter does not require high voltage electrodes, provides much less amounts of lost particles and boasts comparable performance characteristics.

6.2 Simulation of CNV sorting.

One of the key characteristics for sorting system for CNV detection is an enrichment or efficiency factor. This factor can be calculated as:

$$E = \frac{\mathrm{Nsorted}}{\mathrm{Ntotal}} \qquad (7)$$

where N_{sorted} is the number of target beads sorted out of the mixture after a run through the system and N_{tota}l – is the total number of beads after a sort run.

A mixture prepared for CNV detection may consist of 10^6-10^8 beads, while beads with CNV are usually about 0.5-1% of the total amount. This way we have much more detection event than sorting evens. Consequently it justifies a mechanical valve as a sorting device, since its open/close timings are of less importance when we sort rare events. Obviously, we need to take into account its timing characteristics which limit the overall performance of the whole system.

We used two types of valves in our experiments. One with 10ms open/close times (model number 075P2NO12) and one with 0.2ms open/close times (model number INKX051185A). This way in order to ensure its proper operational regime the valves has the upper limits on their switching rates of 50Hz and 250Hz respectively.

The detector's ability to reliably distinguish separate beads relies on the frame rate of the output data. Using LPT output our maximum frame rate is 1KHz, which means we can distinguish beads which are 1ms apart. Though as it was shown above the valves we used had rise/fall times not more than 20ms total. This way our sorting capabilities were limited by the valve performance.

In order to ensure our valves were fast enough for enrichment of the CNV mixed samples we performed a Monte Carlo simulation for different minimum sorting parameters.

We simulated for the mixture containing 2 types of beads. "Blue" beads, which had to be discarded and "red" beads, which had to be sorted. The mixture of beads then went into the system to get sorted. As one of the requirement for the simulation was that the number of red beads in the initial solution had to be 1% or less than the number of blue beads (to match real CNV detection environment) we expected that each sorting event (opening-holding-then closing of the valve) would let through some blue beads in addition to red beads.

On each cycle of pushing the whole batch of the beads through the system we calculated number of sorted beads (red and blue), number of discarded beads (red and blue) and the enrichment factor. The ratio between them had to become lower as we decreased the hold time. Thus, after a full sorting cycle we would have again a mixture of red and blue beads, but this time the enrichment factor had to be higher than before the sorting. Doing the whole sorting sequence multiple times should lead us to the mixture with the enrichment factor of 98-100% which was our goal.

Our simulation program took the following input parameters:

1. Volume of the sample mixed solution, in microliters.
2. Volumetric velocity of the fluid pushed through the system, in microliters per second.
3. Total number of beads in the mixture.
4. Ratio of red beads in the mixture.
5. Hold time of a sorting event.

The arrivals of beads have been simulated to be Poisson distributed.

Since a laminar flow in a cylindrical capillary will have a parabolic velocities profile and our beads are to be fed randomly to the whole opening of the capillary we assumed the same parabolic model for bead velocities spread in the capillary:

$$V(r) = Vc[1 - \left(\frac{r}{R}\right)^2] \qquad (8)$$

where R – is the radius of the capillary, Vc=$\frac{2*Q}{\pi * R^2}$– maximum velocity of the liquid in the capillary (calculated from Q-volumetric velocity of the liquid in the capillary) and r –distance from the center of the capillary to the measuring point.

The distance L between the detection point and sorting point was set to 56mm to emulate the real distance in our setup. This way the following characteristics have been obtained from the spread of beads on 56mm distance in 100microns capillary with 5 microliters per second volumetric velocity of the liquid in the system.

The results of the simulation can be seen on Figure 6.5.

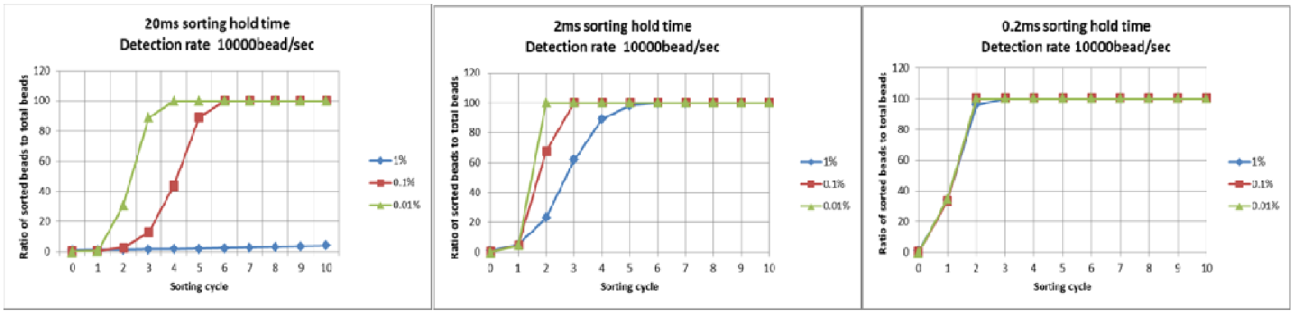

Figure 6.5 Simulation results. Sorting efficiency at different ratios and different hold times for different number of sorting cycles.

3 plots on each graph correspond to 3 different ratios (0.01%, 0.1% and 1%) of red-to-blue beads in the initial sample. The hold times roughly corresponding to the characteristic switching rates of our valves (0.2ms, 2ms and 20ms).

As we can see from the results the best performance was achieved for 0.2ms valve for any initial ratio of red-to-blue beads. Nevertheless 20ms valve was still suitable for lower ratios (less than 0.1%).

6.3 Fixed delay sorting algorithm.

When the laser beam excites fluorescence of the bead, the detected photon count is processed by the FPGA counter. In case if ratio **R** satisfies certain criteria, FPGA sends a control signal to the valve which opens the sorting channel for a short time for collection of sorted beads.

In order to minimize the valve open time and since there is a distance L between the spot where the bead is detected and the T-junction where the bead is sorted, the control signal from the FPGA to the valve has to be delayed. The delay time must be chosen such that by the time when the bead reaches the T-junction, the valve is already opened.

We implemented the following delay scheme:

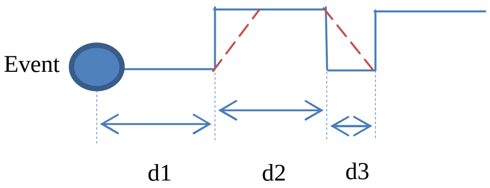

Figure 6.6 Timing diagram. (red dotted lines – real timing characteristics of our valve, thus the need for d3 delay).

- d1, delay time is the time interval FPGA waits before opening the valve after successful comparison of ratios.
- d2, hold time, is the time the valve stays open to guarantee the bead has enough time to get sorted.
- d3, closing time, is the time for the valve to close, since we can’t be sure where a bead goes if it appears at the valve during this time. For d3 interval the FPGA stops processing bead events.

Since d1>>(d2+d3) the system tracks and records all the successful comparison events within d1 time interval from the 1st comparison and raise the output pulse for each of them.

If the distance between consecutive events is MORE than d2+d3 (effective ‘dead time’ of the valve system) each comparison event produces a separate output pulse after d1 delay from its registration.

If the distance between consecutive events is LESS (or equal) than d2+d3 the d2 delay in the output pulse of the 1st event gets prolonged by the time interval between those events in order to sort out both particles in one valve opening period.

Example (Figure 6.7): FPGA registers 3 events. Distance between 1st and 2nd is t1. Distance between 2nd and 3rd – t2. T1<=(d2+d3) and t2>(d2+d3). The system has to produce the rising edge on the output after d1 delay after the 1st event, then hold it for (d2+**t1**) time, then produce the falling edge. Then at time instant (d1+t1+t2) is have to produce the rising edge for the 3rd event.

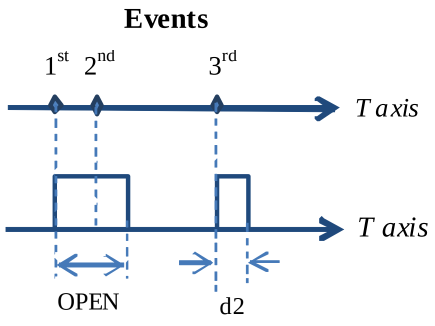

Figure 6.7 Example diagram of control pulses behavior.

We pick 2 groups of channels corresponding to the beads peak wavelengths, then we obtain a ratio of photocounts from both groups of channels as:

$$R = \frac{\sum_{m_0}^{m_1} C_m}{\sum_{n_0}^{n_1} C_n} \qquad (9)$$

where C_m and C_n are photon counts of individual selected channels.

For CNV detection and similar application we need to sort everything which lies outside of the set bounds (see Figure 6.8):

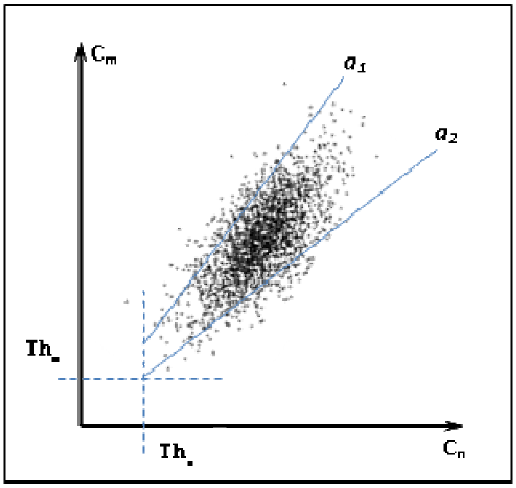

Figure 6.8 Boundary ratios a_1 and a_2 of counts ratio.

Th_m and **Th_n** on the Figure 6.8 above are the noise thresholds since we need to get rid of false positives on the noise floor. They are set individually for each experimental condition, depending on the level of the noise at each particular channel. For example on Figure 6.9 below there's a real life data with a bead peak. Black line represents Threshold value for this channel. It can be seen it's chosen to be way above the noise floor.

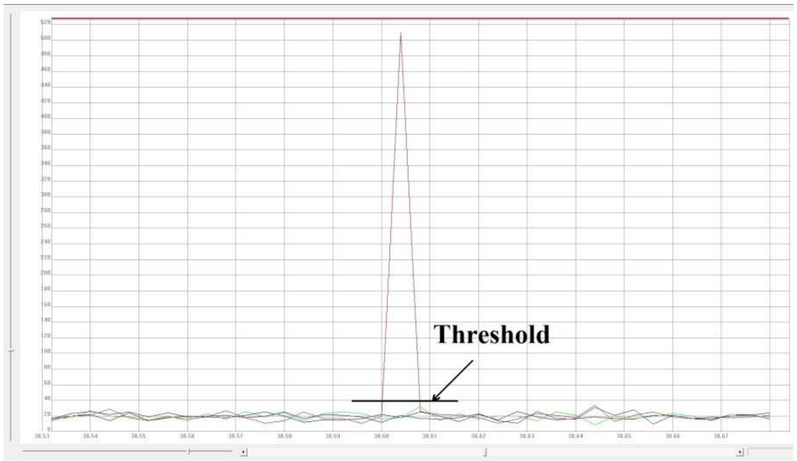

Figure 6.9 Screenshot of the detected bead and channel threshold value.

Specifically for CNV we need to detect anything that differs from 1:1 ratio (normal genes composition between chromosomes). Since there’s some difference between exact amounts of dyes on the beads and there’s a noise in the system (Figure 6.10) that criterion transforms into “we need to sort everything, which lies outside of the set bounds.”

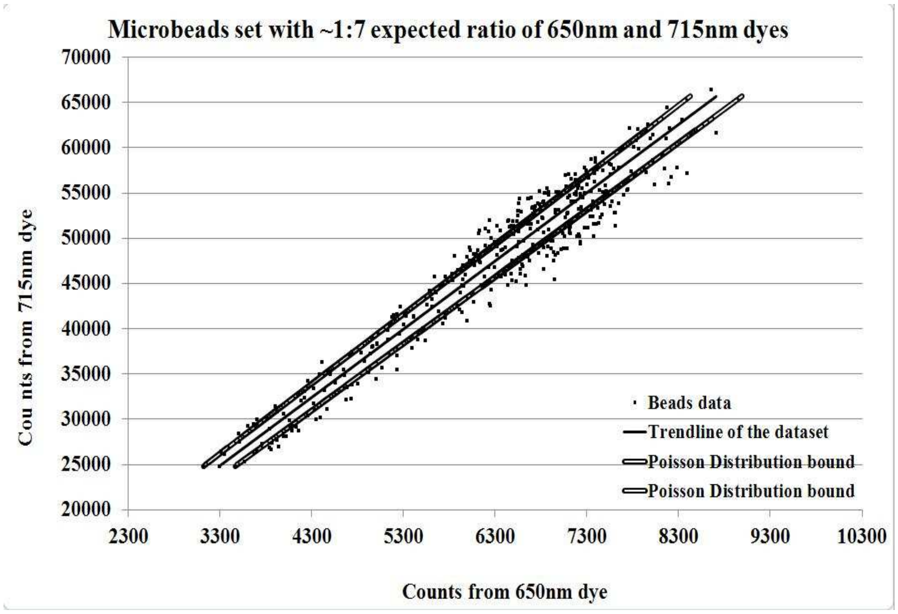

Figure 6.10 Spread of the counts between beads having the same amount of dyes in the system.

6.4 Results with fixed delay.

We did a number of experiments with the valve setup in order to determine its performance and obtain beads velocities profile.

All experiments had original solution of 200-300 beads in 1000ul of water. The beads got pushed through the capillary at such a pressure that we would have 1-2 beads per second, thus ensuring we measure single bead events

We utilized 2 distinct approaches to the experiments:

In first approach we fixed hold time at 50ms and varied delay time until we stopped detecting the beads in sorted vial. The results at Figure 6.11 show quite large spread of arrival times of the beads, having ~75% of them at 25-125ms arrival times range. As can be seen, the bead arrival time varies by about order of magnitude.

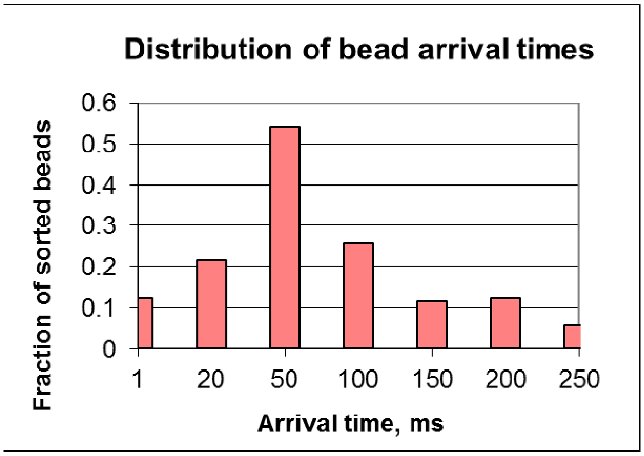

Figure 6.11 Distribution of in 100mkm capillary at pressure 6atm

.On Figure 6.12 we plotted bead velocities corresponding to the obtained arrival times.

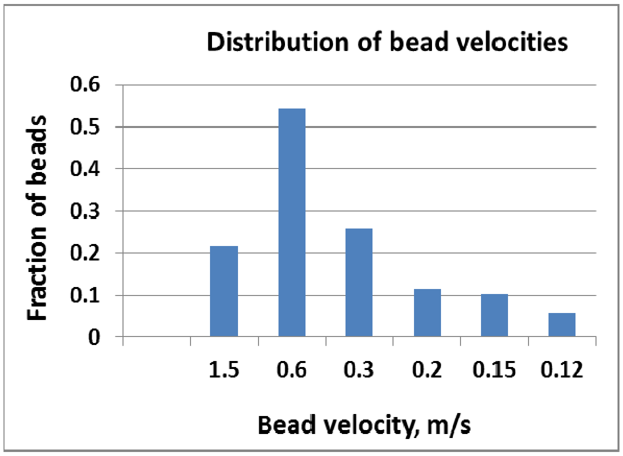

Figure 6.12 Distribution of bead velocities in 100mkm capillary at pressure 6atm.

In the second approach we fixed delay time at 1ms to ensure we would sort all the beads starting from the fastest (figure 6.13). Then we altered hold time to see at what parameters the fraction of sorted bead would 'saturate' thus giving us the upper range of the distribution.

Unfortunately, due to the constraints in our capillary setup about we'd been losing about 10% of all the beads, so 90% of the fraction of sorted beads at 150ms could serve as a good measure of the arrival times for the slowest beads in the capillary.

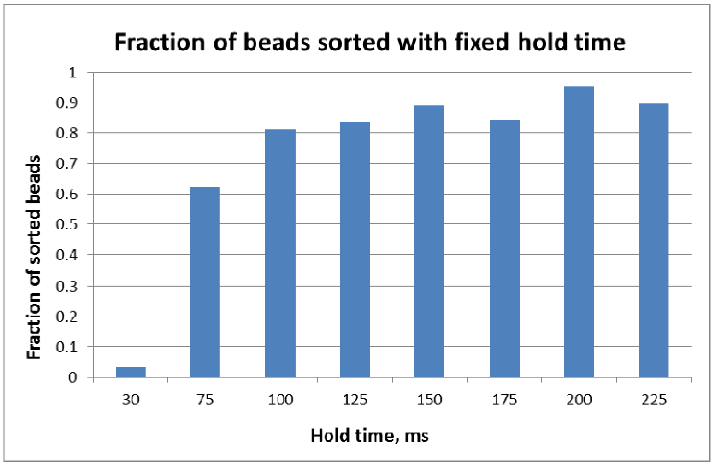

Figure 6.13 Distribution of bead arrival times in 100mkm capillary at different hold times.

6.5 Adaptive delay algorithm.

As it has been shown in fixed delay discussions above beads have a large spread in their velocities due to their special distribution in the capillary. And at no value of delay time we would be able to decrease the hold time down to even 20ms require for efficient CNV sorting. Therefore we need to have a reliable method to determine velocities of each individual bead in order to set its personal delay time. After the delay time is found the only limitation on the performance of the system that will still be needed to take into account is valve switching rates.

This way we can state that the major drawback of the fixed delay mode is that beads in the capillary move at different speeds $\mathbf{V_{BEAD}}$. As a result, time needed for the bead to move from the detection spot to the T-junction varies from bead to bead. To solve the problem, we need to calculate individual delay times d1 $_{BEAD}$ for every bead:

$$\mathbf{d1_{BEAD} = L / V_{BEAD}} \qquad (10)$$

where $\mathbf{V_{BEAD}}$ is velocity of the bead

In order to find $\mathbf{V_{BEAD}}$ we will use the time width of the fluorescent peak which is detected when the bead crosses the laser beam at the detection spot **(**see Figure 6.14 below, which shows a capillary illuminated with laser beam and a bead which moves in the capillary).

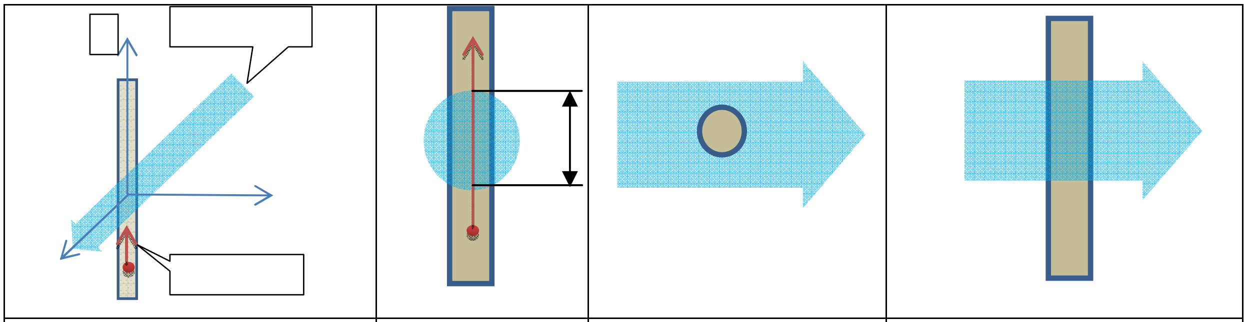

3D positioning of capillary, laser beam, and bead

View A

View B

View C

Figure 6.14 Bead in the capillary.

When the bead crosses the laser beam (see View A) it produces a fluorescence peak of duration $\mathbf{T_{PEAK}}$**.** The peak is detected by PMT and counted by FPGA. In this case

$$\boldsymbol{V_{BEAD}} = \boldsymbol{D}/\boldsymbol{T_{PEAK}} \quad \text{and} \quad \boldsymbol{d1_{BEAD}} = \boldsymbol{L} \times \boldsymbol{T_{PEAK}}/\boldsymbol{D} \qquad (11)$$

It is important to note that for these calculations to stay true we need to ensure that laser spot diameter D will be much greater than the capillary diameter, otherwise due to the circular shape of the spot $\mathbf{T_{PEAK}}$ time intervals for the beads moving at the edges of the capillary will correspond to the lower distance travelled in the laser beam (chords of the circular spot instead of the diameter) thus invalidating velocities calculations.

In order to determine fluorescent peaks produced by the beads we introduce thresholds **Th_m** and **Th_n** for Group of channels #1 and #2 correspondingly **(**Figure 6.15**).**

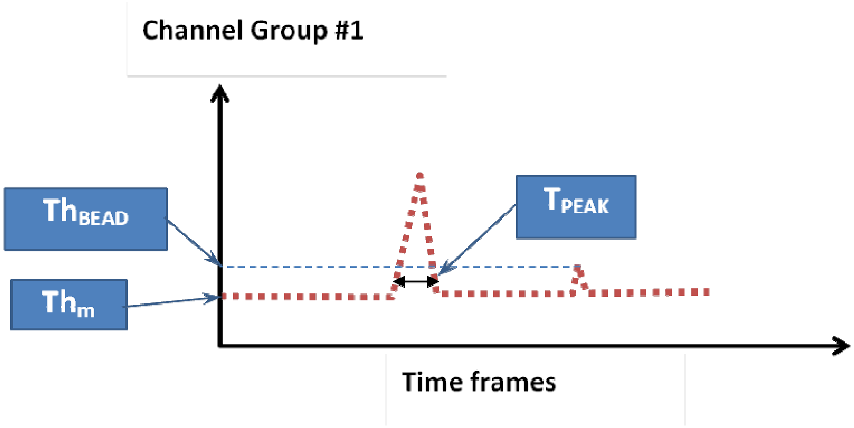

Figure 6.15 Explanation of thresholds.

Based on the thresholds **Th_m** and **Th_n** we find the first data point for which the photon count is above the thresholds in any group of channels, and this will be the **1st** point of the peak **T_{FIRST}**. All subsequent points including the last one above the thresholds (**T_{LAST}**) will be considered as belonging to the peak.

In order to determine **T_{PEAK}** we use the following algorithm: for all data points between the first and the last points of the peak we add together time frames and this will determine time-width of the peak **T_{PEAK}** **(**Figure 6.15**)**.

Our sorting criteria are based on the ratio of fluorescence in two groups of channels. In order to obtain accurate sorting we exclude the beads with small photon count. For that we introduce an additional threshold **Th_{BEAD}.** After subtraction of the background (**$Th_{m,n}$**) we take in consideration only those beads for which the remaining photon count in both groups of channels is larger than **Th_{BEAD}**. All other beads will be neglected.

In order to calculate fluorescent signals **S_1** and **S_2** generated by the bead in Groups #1 and #2, we subtract thresholds **Th_m** and **Th_n** from the entire detected fluorescence and integrate the entire fluorescence detected during the pulse:

$$S_1 = \sum_{t=T_{FIRST}}^{t=T_{LAST}} \left\{ \left[\left(\sum_{m_0}^{m_1} C_m \right) - Th_m \right]_t \right\} \tag{12}$$

$$S_2 = \sum_{t=T_{FIRST}}^{t=T_{LAST}} \left\{ \left[\left(\sum_{n_0}^{n_1} C_n \right) - Th_n \right]_t \right\} \tag{13}$$

If $S_1 > Th_b$ **and** $S_2 > Th_b$ **then and only then** we proceed calculate the ratio **R** for the pulse as $\mathbf{R} = \frac{\boldsymbol{S_1}}{\boldsymbol{S_2}}$

Next we use the following a similar criterion as in fixed delay case to determine a sorting event: sorting must occur if $\boldsymbol{R} > a\mathbf{1}$ or $\boldsymbol{R} < a\mathbf{2}$.

After we determined that the current bead has to be sorted we go on with calculating delay time ($d1_{BEAD}$) until FPGA raises sorting control signal for this particular bead.

In order to determine delay time $\mathbf{d1_{BEAD}}$ we do the following:

- In the program we set the distance **L** from detection point to the T-junction;
- For each sorting event we will calculate the delay time $\mathbf{d1_{BEAD}}$ as**:**

$$\boldsymbol{d1_{BEAD}} = \frac{\boldsymbol{L \times T_{PEAK}}}{\boldsymbol{D}} \tag{14}$$

Next important thing is that the order in which we detect the beads at the **detection spot** may change when the beads reach the **T-junction** (this is because on the distance **L** those beads which have higher velocity can overtake the beads which have lower velocity).

Therefore, from the point of view of the **valve** it looks like commands $\mathbf{Valve_{OPEN}}$ and to $\mathbf{Valve_{CLOSE}}$ may follow in an order which we don’t know in advance (see Figure 6.16).

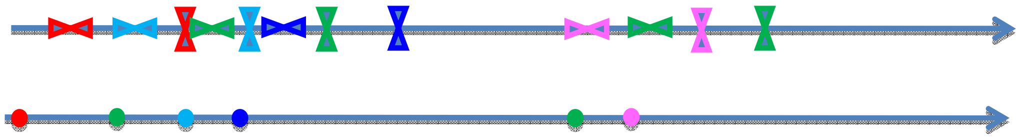

Figure 6.16 Diagram of valve control signals for a sequence of beads.

Valve open/close algorithm we came up with is the following:

- We put in chronological order and save as a **Time Array** those times which correspond to $\mathbf{T_{OPEN}}$ and $\mathbf{T_{CLOSE}}$ = $\mathbf{T_{OPEN}}$ +**d2** for every individual bead
- We introduce a parameter "**VALVE**" (either equal to **1** or **0)** for the valve **"open" and "close"** states correspondingly. (The valve in our system is **normally closed).**
- We introduce a parameter '**Last open**' to track the timestamp of the last '**open'** event happened.
- Parameter "**VALVE**" is checked at every frame:

  - **<u>If</u> VALVE=0 (close) <u>and</u>** for the current frame we hit $\mathbf{T_{OPEN}}$ **<u>then</u>** we will do the following:
    - a) Send command "**Valve** $\mathbf{_{OPEN}}$**"**
    - b) put **VALVE=1**
    - c) set '**Last open**'= $\mathbf{T_{OPEN}}$
    - d) set new $\mathbf{T_{CLOSE}}$**=** $\mathbf{T_{OPEN}}$**+d2**
    - e) add this additional $\mathbf{T_{CLOSE}}$ to **Time Array** and sort the array

  - **<u>If</u> VALVE=1 (open) <u>and</u>** we hit $\mathbf{T_{OPEN}}$ for the current frame, **<u>then</u>** we will do the following:
    - f) set '**Last open**'= $\mathbf{T_{OPEN}}$
    - g) set new $\mathbf{T_{CLOSE}}$**=** $\mathbf{T_{OPEN}}$**+d2**
    - h) add this additional $\mathbf{T_{CLOSE}}$ to **Time Array** and sort the array

- **If VALVE=1 (open) and** we hit $\mathbf{T_{CLOSE}}$ for the current frame, **then** we will do the following::
    - i) **if** $(\mathbf{T_{CLOSE}} - \textbf{"Last Open"}) < \ d2$ **then** we keep **VALVE=1**
    - j) **if** $(\mathbf{T_{CLOSE}} - \textbf{"Last Open"}) = \ \mathbf{d2}$ **then**
        1. **if** $\mathbf{T_{CLOSE}}$**+d3** is **larger** than **the next** $\mathbf{T_{OPEN}}$ **then** we keep **VALVE=1**
        2. **if** $\mathbf{T_{CLOSE}}$**+d3** is **smaller then the next** $\mathbf{T_{OPEN}}$ we
            - set **VALVE=0**
            - send command **"Valve** $\mathbf{_{CLOSE}}$**"**

Data recording system had to change to accommodate the requirement for precise calculations of T_{peak} values.

In LPT mode we implemented a specific mode of counts integration. We're still limited by 1kHz LPT output rate, but we use the framerate value for the whole procedure of calculating ratios and pulse widths. Then the data points have to be summed by the factor of $\frac{\text{Framerate}}{\text{1kHz}}$ points to create 1kHz LPT output stream.

In USB mode we use the current framerate value for both the integration intervals and output data stream rate.

6.6 Results of adaptive delay mode.

One of the benefits of the adaptive delay mode is that now we have a direct way to determine velocities profile of the fluorescent particles with great precision. T_{peak} values obtained at each measurement are transmitted instead of 1^{st} channel values in microseconds format.

We used that data for multiple runs to collect a statistics of bead velocities in the capillary. As I mentioned before the key requirement for accurate measurements of the bead velocities in the capillary using adaptive delay software was to have the laser spot diameter much larger than the diameter of the capillary. Since our laser spot was ~80microns is diameter we could not use 100micros capillary for the measurement. All the following results have been made with 50microns capillary instead.

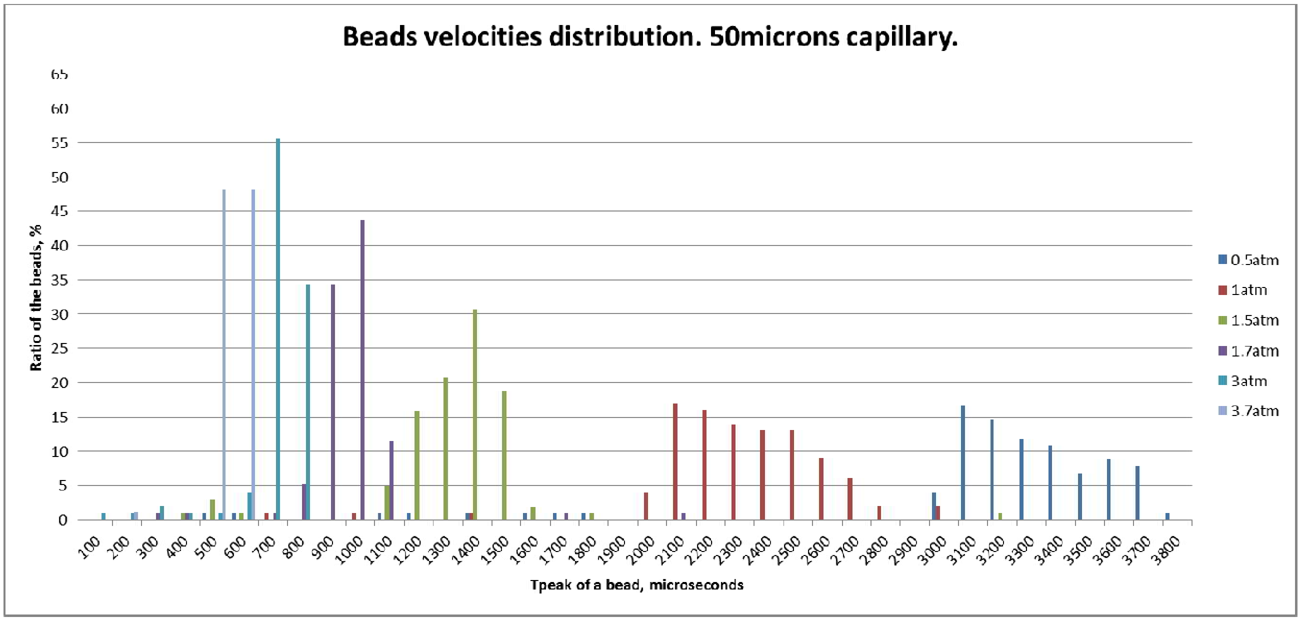

Figure 6.17 Beads velocities distribution.

Figure 6.17 contains Tpeak results for 6 measurements for different pressures and thus volumetric velocities. The applied pressure varied from about 0.5 atmospheres (rightmost graph) to 3.7 atmospheres (leftmost).

Actual velocities of the beads can be found dividing 80microns (laser spot diameter) by Tpeak value. So for 2.5 atmosphere pressure (forth from the right on Figure 6.17) median velocity of the beads is 80/1000=0.08m/sec.

As we can see as the pressure increases velocities go up and at the same time the spread of velocities decreases as if the beads change their configuration in the capillary depending on the pressure. This behavior requires more investigations, for now it coincides with the results for the beads distribution in the capillary we obtained for CCD camera experiments.

To test the accurateness of the values we obtained for the FPGA software we assembled a setup with CCD camera(figure 6.18):

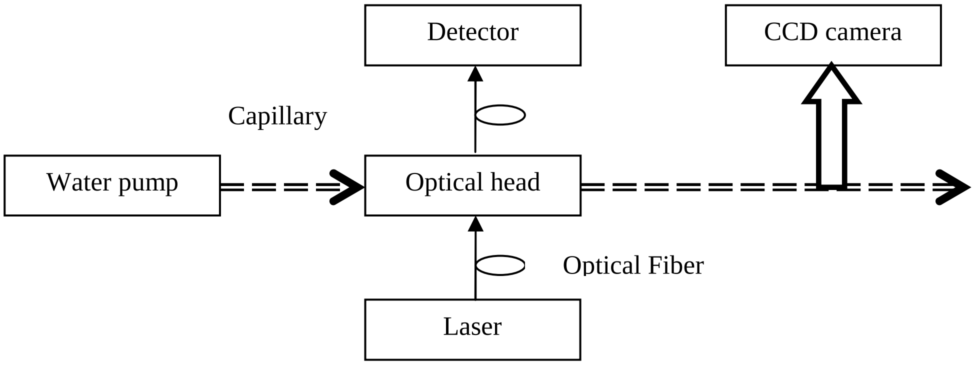

Figure 6.18 Test setup for validating beads velocities.

We used a CCD camera with fixed frequency of the internal trigger to make snapshots of the beads in the capillary. By counting the number of pixels in the two subsequent snapshots we could measure distance intervals in individual beads locations, separated by fixed and known time intervals.

Velocities measurements with the camera and Tpeak calculations matched within measurement error, thus giving us the confirmation that the software is capable of measuring velocities of fluorescent particles with great degree of precision.

Then we used this method to make sure that operation regime of the valve doesn’t affect beads before reaching T-junction or otherwise behavior of the system will be unpredictable and probably unmanageable. To test for that we used a function generator to produce a train of pulses with different duty cycles (10% and 50%) and different frequencies (1Hz, 10Hz and 50Hz) that emulated different modes of operation of the valve.

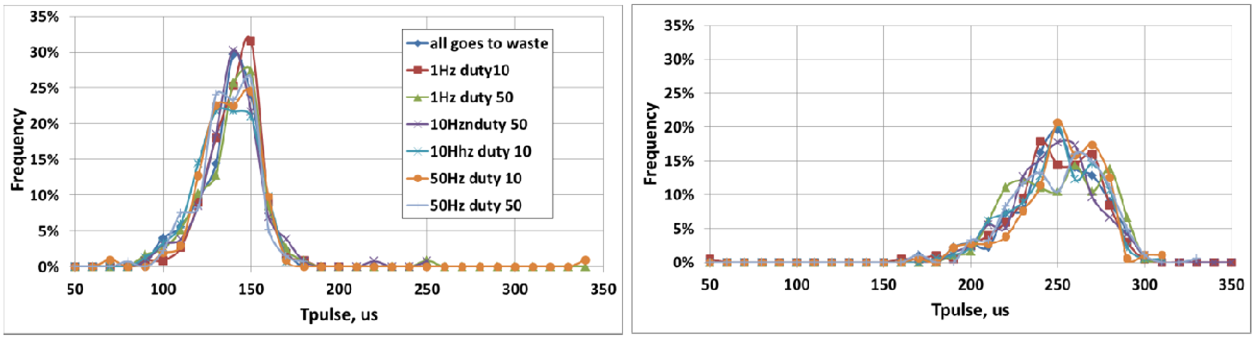

Figure 6.19 Tpeak values for different test pulse sequences.

The results (Figure 6.19) clearly showed that there's a slight valve-induced variance is beads velocities, though its impact on the performance of the system is minimal thus justifying usage of mechanical valves for sorting of micro-particles.

Nevertheless it's very important to measure how much difference variances of the velocities of the beads can affect the system.

I performed a simulation of the valve sorting system using actual bead velocities profile data from the measurements on Figure 6.17 instead of theoretical parabolic distribution used previously.

The goals of the simulation were:

- to determine necessary valve hold time values for different additional variances of the beads velocities in the capillary and for different distances L from detection point to the T-junction, since both these parameters are crucial for actual distributions of the beads;
- to quantitatively compare effectiveness of fixed-delay sorting method with more promising adaptive delay method.

For simulation parameters I used 1000mkl beads solution, which was pushed through the capillary at 0.628mkl per second volumetric velocity (to match 2.5 atmospheres velocities profile data). The sample size was 100000 beads. The criterion for optimal hold time value was chosen in such a way that that value had to be the minimum hold time to achieve 1% of bead lose per soritng cycle. This way 99% of the beads in the initial sample would be sorted and appear in the sorting output via).

First set of simulations used a fixed value of the distance L=17mm (to match the distance in our actual system) between the detection point and T-junction. Then bead arrival times have been simulated using Poisson statistics, which have been assigned a velocity from the distribution of the Figure 6.17. Then each individual velocity was randomly altered within a set of ranges. Starting from 0% variance (unmodified randomly assigned velocities from the profile) the simulation goes up to 25% difference in velocity from the original (actual value was picked randomly from 75% to 125% of original velocity). The values of the minimum hold times necessary to achieve 1% of bead loss after a sorting cycle with each velocity variance have been obtained separately for fixed delay mode and adaptive delay mode.

For better accuracy of the results delay times (both fixed and adaptive) have been chosen to indicate the middle point of the hold time interval. For instance if delay time was 100ms and hold time 50ms the valve opened at 100-50/2=75ms delay and stayed open until 100+50/2=125ms time.

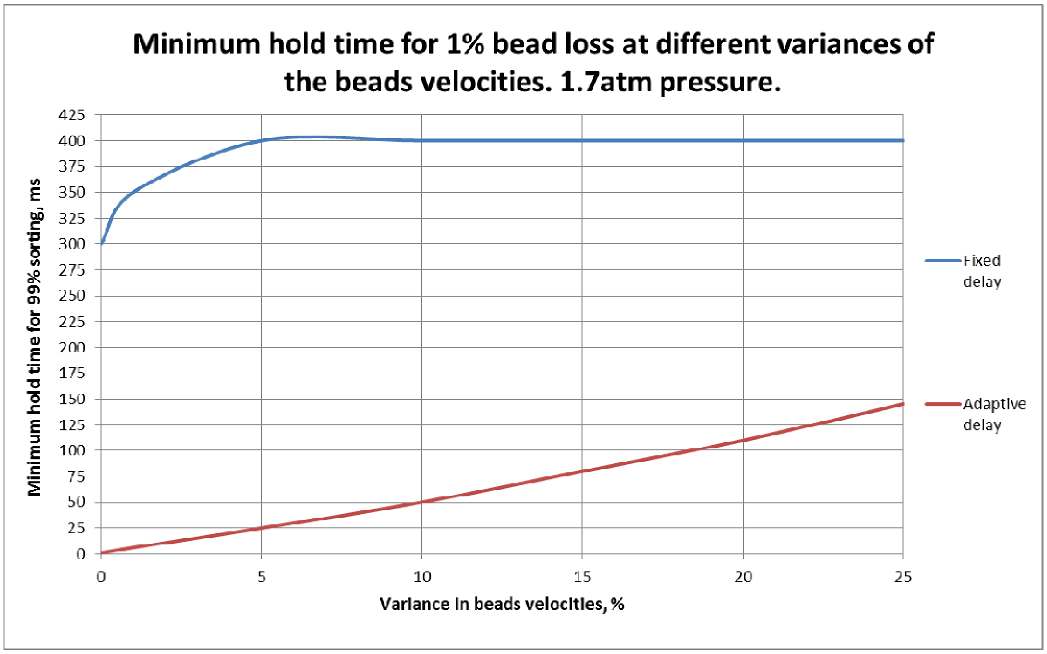

Figure 6.20 Hold time for 1% bead loss at different variances of the beads velocities at 1.7atm pressure.

The results are shown on Figure 6.20. It can be seen that the adaptive delay method (red plot) has a clear advantage over fixed delay one, which is especially drastic at lower variances (0%-5%), where fixed delay requires at least 300ms hold time to achieve 99% sorting efficiency and adaptive delay is perfectly viable at 25ms and below.

The next important thing to simulate was find out how exactly different distances L affect minimum hold times for both methods. The variance was set at 10%, which was the upper bound of experimental results on Figure 6.19. Then the distance was changed between 0mm (instant sorting) and 25mm. The results are shown on the Figure 6.21:

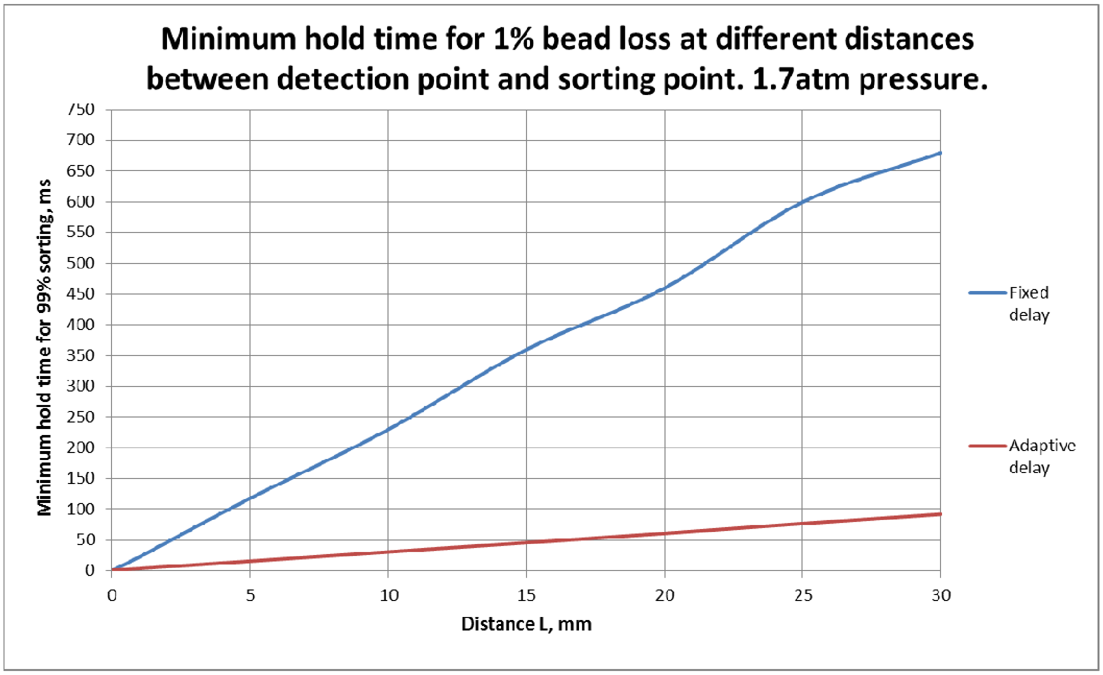

Figure 6.21 Hold time for 1% bead loss at different distances L at 1.7atm pressure.

Once again we can see a huge advantage of adaptive delay method over fixed delay one. Even at 25mm distance adaptive delay needed just 90ms hold time to guarantee 99% sorting, while fixed delay required about 700ms! It can be seen from the plot that the characteristics are almost linear, though at different slopes. This way, advantages of the adaptive delay mode become even higher as the distance increases.

In the result of the simulation there was a clear and substantial advantage of the adaptive delay method in almost any conditions. And the simulation confirmed that for low variance conditions (<10%) with distance between detection and sorting point at 15mm or less, adaptive delay mode can be used to reliably sorting more than 99% of all the beads.

Figures 6.22 and 6.23 contain the same simulation results for adaptive and fixed delay comparisons, but at a higher pressure and volumetric velocity (3.7atm versus 1.7atm).

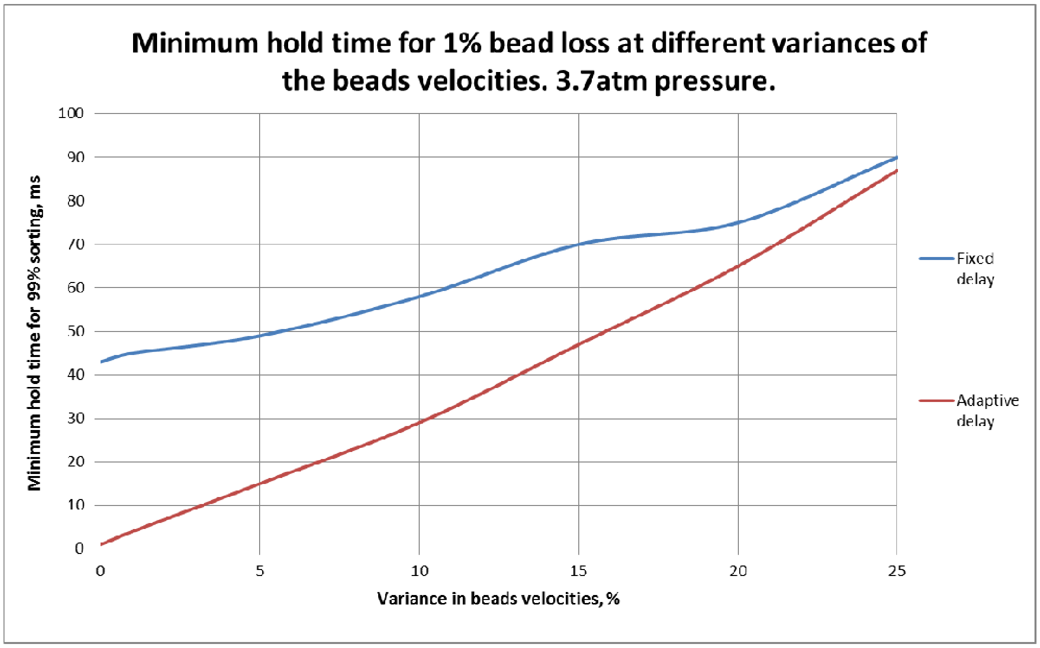

Figure 6.22 Hold time for 1% bead loss at different variances of the beads velocities at 3.7atm pressure.

The beads spread is much lower at 3.7atm pressure than it was at 1.7atm (Figure 6.17) since the velocities are much higher. Therefore requires minium hold times for fixed delay and adaptive delay on Figure 6.22 are much closer that in 1.7atm case and as variance increases their perfirmances match.

Distance versus minimum hold time plot (Figure 6.23) still shows clear benefits of using adaptive delay though the slopes of the graphs are closer than in 1.7atm case.

This way we can state that adaptive delay has a significant advantage over fixed delay case at different volumetric velocities of the beads and different spreads of their velocity profiles.

For extreem cases like very high variance of bead velocities and very low distance betwee detection and sorting points (for instance in case of micro-chip based sorters) fixed delay is still a viable methods of achieving required sorting performance.

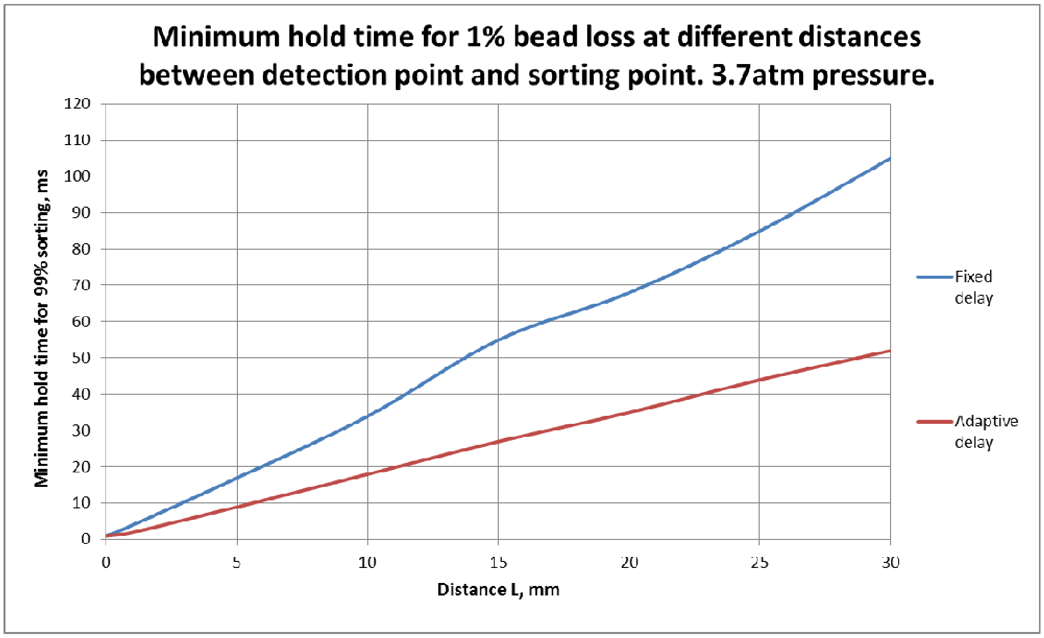

Figure 6.23 Hold time for 1% bead loss at different variances of the beads velocities at 3.7atm pressure.

6.7 Conclusion.

We developed a bead sorter device having outstanding characteristics, discussed its performance and showed its application for CNV detection. The sorter can boast low to none bead loss, multiple type of sorting objects using the same setup, high detection and sorting speeds, small size and relatively low cost.

Extensive simulation of different sorting algorithms showed that reducing distance between detection point and sorting point and increasing applied pressure and thus volumetric velocities of the beads led to much lower required hold time of the sorting valve, which allowed more sorting events per second and improved overall performance of the sorter.

Additionally our adaptive delay sorting method proved to be a considerable improvement over more traditional fixed delay sorting and justified 10ms sorting events.

6.8 Future work.

There’s an important experiment that I have to leave for the future work since it requires a special setup and equipment which is not available at the moment.

As we showed above the method provides quite reliable statistics for beads velocities profile in the capillary. Though for efficient sorting we need to explicitly test adaptive delay method to make sure that each time we calculate a specific delay for each bead that particular bead will appear at the junction right after the delay.

This way I propose the following setup (Figure 6.24):

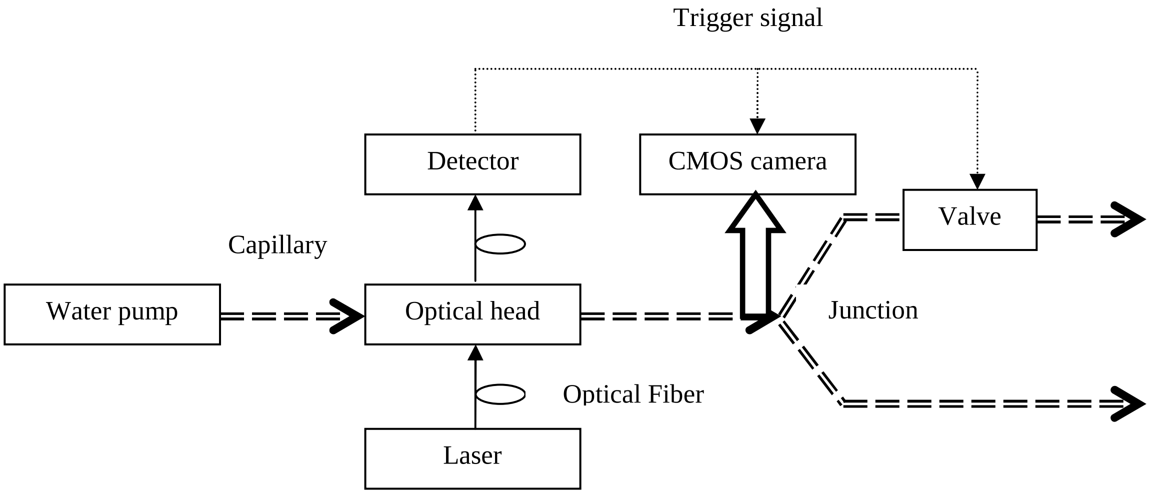

Figure 6.24 Test setup for validating adaptive delay using a CMOS camera.

It is similar to the test setup for the velocities (Figure 6.18), but it has a real valve, real junction and a camera looking directly in the junction.

One of the important requirements to the setup is to have a very fast CMOS camera, since all CCD cameras available on the market have their frames per second limited at about 100-500. But for the beads is the capillary moving at characteristic linear velocities of about 1 meter per second the optimal exposition times have to be in the range of 5-15microseconds. That range requires a scientific CMOS camera (for instance Redlake MotionXtra HG-XR 100000fps camera and similar).

Then the detector will calculate individual delay times for the beads and provide trigger signal after the delay time to both the camera (to take a snapshot of the junction) and the valve (to sort the bead).

Using this setup we'll be able see the beads near the junction at the precise moment just before there're sorted by the valve. And this way ensuring the delays are indeed suitable for each bead.

CONCLUSION

We have developed a universal fiberized single photon sensitive spectrometer based on 32-channel PMT sensor and a method for highly accurate and experimental determination of composition of mixtures containing multiple fluorescent components with overlapping spectra. The spectrometer fully satisfy the goal we set in the beginning: linearity hold up to 60-70 million counts per second without additional correction and up to 100 million counts per second with ~20% count loss, which can be corrected by post-processing.

Comparison between Monte-Carlo simulated and actual experiments results have demonstrated excellent agreement between them, which supports other evidences that our detector counts strictly follow Poisson distribution. Another conclusion we deduced from the experiments is the device non-linear output and deviation of Poisson distribution happens simultaneously.

We believe that due to an extremely high sensitivity of the photon detection in conjunction with the method for highly accurate color decomposition, the developed spectrometer may be very useful for detection and decoding of multiple color codes and it can be used in various applications which require highly accurate identification of biological samples labeled with multiple quantum dots.

BIBLIOGRAPHY

[1]. Nicewarner-Pena, S. R.; Freeman, R. G.; Reiss, B. D.; He, L.; Pena, D. J.; Walton, I. D.; Cromer, R.; Keating, C. D.; Natan, M. J. “Submicrometer metallic barcodes,” Science 2001, 294, 137-141.

[2]. Dejneka, M. J.; Streltsov, A.; Pal, S.; Frutos, A. G.; Powell, C. L.; Yost, K.; Yuen, P. K.; Muller, U.; Lahiri, J. “Rare earth-doped glass microbarcodes,” Proc. Natl. Acad. Sci. U.S.A. 2003, 100, 389-393.

[3]. Grondahl, L.; Battersby, B. J.; Bryant, D.; Trau, M. “Encoding Combinatorial Libraries: A Novel. Application of Fluorescent Silica Colloids,” Langmuir 2000, 16, 9709-9715.

[4]. Braeckmans, K.; de Smedt, S.; Roelant, C.; Leblans, M.; Pauwels, R.; Demeester, J. Nat., “Encoding microcarriers by spatial selective photobleaching,” Mater. (2003), 2, 169-193.

[5]. Mulvaney, S. P.; Musick, M. D.; Keating, C. D.; Natan, M. J., “Glass-coated, analyte-tagged nanoparticles: A new tagging system based on detection with surface-enhanced Raman scattering,” Langmuir 2003, 19, 4784-4790.

[6]. Gao, X.; Nie, S., „Doping Mesoporous Materials with Multicolor Quantum Dots” *J. Phys. Chem. B*, 2003, *107* (42), pp 11575–11578

[7]. Ful, A., Gu, W.; Larabell, C.; Alivisatos, A.P. “Semiconductor nanocrystals for biological imaging”; Current Opinion in Neurobiology 2005, 15:568–575

[8]. Gao X., Nie S., “QD-encoded mesoporous beads with high brightness and uniformity: rapid readout by flow cytometry“ Analytical Chemistry,76, 2406-2410, 2004

[9]. L. Alaverdian, S. Alaverdian, O. Bilenko, I. Bogdanov, E. Filippova, D. Gavrilov, B. Gorbovitski, M. Gouzman, G. Gudkov, S. Domratchev, O. Kosobokova, N. Lifshitz, S. Luryi, V. Ruskovoloshin, A. Stepukhovich, M. Tcherevishnick, G. Tyshko, V. Gorfinkel, “A family of novel DNA sequencing instruments based on single photon detection” Electrophoresis 23, pp. 2804-2817, 2002.

[10]. A. Tsupryk, I. Tovkach, D. Gavrilov, O. Kosobokova, G. Gudkov, G. Tyshko, B. Gorbovitski and V. Gorfinkel, “Ultra sensitive sensor with enhanced dynamic range for high speed detection of multi-color fluorescence radiation,” Biosensors and Bioelectronics
Volume 23, Issue 10, Pages 1512-1518

[11] Kay, S. “Fundamentals of statistical signal processing: estimation theory” Prentice Hall, New Jersey, 1993, 597p.

[12] Fu A. Y., Spence C., Scherer A., Arnold F. H., Quake S. R., “A microfabricated fluorescence-activated cell sorter” Nature Biotechnology 17, pages 1109 – 1111, 1999

[13] Davey H. M., Kell D. B., "Flow cytometry and cell sorting of heterogeneous microbial populations: the importance of single-cell analyses." Microbiol. Mol. Biol., vol. 60 no. 4 641-696, 1996

14] Jiang, Z., Llandro, J., Mitrelias, T., Bland, J.A.C, "An integrated microfluidic cell for detection, manipulation, and sorting of single micron-sized magnetic beads", Journal of Applied Physics, Volume 99, Issue 8, 2006

[15] Tondra, M., Granger, M., Fuerst R., Porter, M., "Design of integrated microfluidic device for sorting magnetic beads in biological assays", Magnetics, IEEE Transactions, Volume 37, Issue 4, 2001

[16] A. Wolff, I. R. Perch-Nielsen, U. D. Larsen, P. Friis, G. Goranovic, C. R. Poulsen,

J. P. Kutter and P. Telleman, "Integrating advanced functionality in a microfabricated high-throughput fluorescent-activated cell sorter" Lab Chip**,** 3, 22-27, 2003